NASA TECHNICAL NOTE

NASA TN D-7998

NASA TN D-7998

EXPERIMENTAL INVESTIGATION OF A MACH 6 FIXED-GEOMETRY INLET FEATURING A SWEPT EXTERNAL-INTERNAL COMPRESSION FLOW FIELD

Marvin G. Torrence

Langley Research Center
Hampton, Va. 23665

NATIONAL AERONAUTICS AND SPACE ADMINISTRATION • WASHINGTON, D. C. • OCTOBER 1975

EXPERIMENTAL INVESTIGATION OF A MACH 6 FIXED-GEOMETRY INLET FEATURING A SWEPT EXTERNAL-INTERNAL COMPRESSION FLOW FIELD

Marvin G. Torrence
Langley Research Center

SUMMARY

An investigation of a fixed-geometry, swept external-internal compression inlet has been conducted at a Mach number of 6.0 and a test-section Reynolds number of 1.55×10^7 per meter. The test conditions were constant for all runs with stagnation pressure and temperature at 20 atmospheres and 500 K, respectively. Tests were made at angles of attack of -5°, 0°, 3°, and 5°. Measurements consisted of pitot- and static-pressure surveys in the inlet throat, wall static pressures, and surface temperatures. Boundary-layer bleed was provided on the centerbody and on the cowl internal surface.

The inlet performance was consistently high over the range of the angle of attack tested, with an overall average total pressure recovery of 78 percent and corresponding adiabatic kinetic-energy efficiency of 99 percent. The inlet throat flow distribution was uniform and the Mach number and pressure level were of the correct magnitude for efficient combustor design. The utilization of a swept compression field to meet the starting requirements of a fixed-geometry inlet produced neither flow instability nor a tendency to unstart.

INTRODUCTION

Vehicles capable of hypersonic velocities (especially those propelled by airbreathing engines) have been the subject of considerable interest and study in recent years (ref. 1). At the present time the flight Mach number range from 4 to 10 is of prime interest to researchers in aeronautics. The effect of high stagnation temperatures on rotating parts and the attendant structural problems eliminate turboengines from the hypersonic flight regime, leaving the scramjet (supersonic combustion ramjet) as the only acceptable airbreathing engine for these speeds. One such vehicle meeting the aerodynamic and propulsion system requirements at hypersonic speeds is depicted conceptually in figure 1. This concept was developed by New York University personnel (ref. 2) sponsored by the National Aeronautics and Space Administration (NASA) university research Grant No. 33-016-131.

The propulsion system is an integral part of the vehicle; the large forebody is utilized as an inlet compression surface (centerbody), and the afterbody serves as part of the exhaust nozzle. The inlet cowl is swept and wrapped around the vehicle in an arc of 120°. This particular engine design uses the thermal-compression concept (ref. 1) to aid in the supersonic combustion process. The thermal compression is achieved by utilizing instream fuel injectors that are located in the inlet throat in such a manner as to intercept and cancel initial internal shocks and to produce additional compression with combustion-induced shocks. Because of the complexity of the internal flow field, fuel injector design relies heavily on accurate experimental data.

With these considerations in view, a scaled model of the inlet was tested for a detailed study of the external and internal flow fields. Since duplication of flight conditions for this configuration is not possible in wind-tunnel testing, final design must depend heavily on analytical prediction and verification of these analytical methods with test data. In a previous experiment (ref. 3), a 1/4-scale version of the present model centerbody was tested at Mach numbers of 6 and 8.5. Test data from this experiment (ref. 3) were used successfully to verify the accuracy of an existing three-dimensional (3-D), near-characteristics program using the reference plane method (refs. 4 and 5); the program was used to predict the external flow field. The tests reported here were made at a Mach number of 6 with a constant Reynolds number. The variables were the angle of attack (-5°, 0°, 3°, and 5°) and with boundary layer tripped and untripped. Measurements consisted of surface temperature, surface pressure, and static- and pitot-pressure surveys in the throat region. Visual observation was obtained by a schlieren system. Inlet starting, stable operation, and the measurement of throat flow conditions at $M_\infty = 6$ were the primary objectives of the test program. Data analysis included detailed mapping of flow parameters at the throat station and determination of inlet-performance estimates based on mass weighted averages of these parameters.

SYMBOLS

A	cross-sectional area, meters^2
M	Mach number
$\dot{m}$	mass flow, kilograms/second
p	absolute pressure, newtons/meter^2

T	absolute temperature, degrees kelvin
X	longitudinal coordinate (longitudinal distance from leading edge of component under consideration; in respective planes), centimeters
Z	distance from centerbody, nondimensionalized by local throat height
α	angle of attack, degrees
θ	angle defining centerbody radial plane, degrees (see fig. 2(d))
η_D	total pressure recovery, $p_t/p_{t,\infty}$
η_{KE}	adiabatic kinetic-energy efficiency

Subscripts:

aw	adiabatic wall value for turbulent flow
isen	isentropic field conditions
max	maximum or limiting value
ref	reference flow conditions
T	values at the throat station
t	total or stagnation conditions
w	wall
∞	free-stream conditions
2	conditions after normal shock

Dots over symbols denote derivatives with respect to time. Bars over symbols denote arithmetic average values.

APPARATUS AND PROCEDURE

Model

The inlet design (fig. 2) is for operation over a Mach number range from 4 to 10 with a starting capability as low as Mach 3.5. The inlet features a low internal contraction ratio of 2.51 and an external contraction ratio of 2.88 for an overall geometric contraction ratio of 7.23. (See fig. 2(c).) The shock-on-lip or full-capture design Mach number is 10 at $\alpha = 0^{\circ}$. The present tests were made at Mach 6 which is considered a representative point in the hypersonic regime for the current interest in vehicle applications.

Design philosophy.- A sketch of the model tested in this investigation is shown in figure 2(a). The 7.5° half-angle cone spike is followed by a flared elliptic centerbody with the major axis in the vertical plane. The elliptic cross section is permitted to grow in such a manner as to generate an isentropic compression surface in any radial plane emanating from the longitudinal center line (refs. 2 and 3). The effect of the elliptic cross section is to delay compression in the outboard planes such that the captured flow is at the same pressure along the swept-cowl leading-edge station. The swept compression and cowl ease the starting requirements for the fixed-geometry configuration. The oblique initial shock is ingested gradually rather than suddenly as in the case of the starting of an axisymmetric inlet where the initial shock is normal. In addition to the advantage gained in starting, the sweep gives some aid in the leading-edge heating problem.

Model description.- The test model is a 3-D, mixed-compression (external and internal), fixed-geometry inlet with a swept-cowl leading edge and a swept throat line. A slot-injection boundary-layer trip is located at the 11.4-cm station with an injected flow angle of 5° to the cone surface. The flow rate and the pressure used to choke the slot flow were selected on the basis of the experimental data reported in reference 6. Because of the low test Reynolds number (approximately one-tenth of the design flight value), a large boundary-layer thickness relative to the throat height is developed and is ingested by the inlet if boundary-layer removal is not accomplished. Boundary-layer bleed is provided for by flush holes on the inner surface of the cowl and by a throat insert forming a scoop on the centerbody as shown in figure 2(a). During model assembly the boundary-layer scoop passage was discovered to trail off gradually to a zero area at the left sidewall. In the integrated vehicle-engine configuration (fig. 1) the inlet cowl is wrapped around the centerbody in a 120° segment with symmetry about the vertical plane. An initial wedge on the inner cowl surface is 2° upward relative to the horizontal center line in each radial plane and extends for a constant length of 5.08 cm from the leading edge. This wedge is followed by a horizontal surface and then by a 10° expansion. The sidewall

leading edges in the $\pm 60^{\circ}$ radial planes are swept 45° from the cowl to the centerbody and diverge 10° longitudinally. The throat of this type of inlet is a thin annular sector with a relatively small throat height. In scaling the model to a size large enough to obtain useful measurements in the throat, the overall model size becomes very large because of the requirement of vehicle flow-field simulation by the centerbody. In order to meet the tunnel starting requirements, the model cowl is limited to a 75° segment with the 15° segment to the right of the vertical plane included as a symmetry check. The model coordinates are defined by the mathematical equations and tabulated values in reference 2.

Instrumentation

Surface measurements.- Wall static pressures were measured by six pressure transducers (four 34.47×10^3 N/m^2 and two 68.94×10^3 N/m^2) used in conjunction with multiport rotary valves. Static orifice locations are tabulated in figure 3(a). A clearer reference to orifice orientation can be made from figures 2(b) and 3(c). Centerbody statics are in radial planes from the vertical ($\theta = 0^{\circ}$) to the most outboard plane ($\theta = 60^{\circ}$) in increments of 15°. These statics are shown numbered in figure 3(c). The inner surface of the cowl has wall orifices in the same radial planes. Wall statics on the forecone are located in planes of 0°, 90°, 180°, and 270°. Surface temperatures were measured by chromel-alumel thermocouples. Forecone thermocouples are in planes of 45°, 135°, 225°, 315°, and in the 0° plane on the elliptic centerbody. Thermocouples are also located in outboard planes on the cowl inner surface and centerbody downstream of the boundary-layer scoop.

Survey measurements.- The inlet throat region was surveyed by four pitot- and static-pressure rakes; the pitot rake installation is shown in figures 3(b) and 3(c). The center-line rake consisted of a symmetric array of nine probes, and the outboard rakes contained five probes each with the probe tips located along the swept throat line. The outside diameter of each probe was 1 millimeter; the center-to-center spacing of the probes was 6.4 millimeters. The static-pressure survey rakes were similar except that rakes 2, 3, and 4 had the second and fourth probes removed in order to prevent shock interference from adjacent probes. Each rake was mounted on a gear-driven post and simultaneous movement was assured by the linkage at the rear of the model (fig. 3(c)). Pitot pressures were measured on individual 345×10^3 N/m^2 transducers and static survey pressures were measured by Baratron pressure cells. (See ref. 7.) All data were recorded by a Beckman data acquisition system and were reduced to ratio form. Pressures and temperatures were nondimensionalized by the free-stream static pressure and stagnation temperature, respectively. A schlieren system was used to observe and photograph the flow in the vertical plane.

Test Procedures and Conditions

A detailed description of the test facility used in this investigation is given in reference 7. The test conditions in the 51-cm square test section were constant for all data runs with a free-stream Mach number of 6, a stagnation pressure and temperature of 20 atmospheres and 500 K, respectively, and a corresponding Reynolds number of 1.55×10^7 per meter. A typical test run included: an initial preheat of the test section and model; verification of the tunnel and inlet start by schlieren observation; and finally an increase in the stagnation tunnel conditions up to preselected values prior to data recording. Pressure surveys were always made from centerbody to cowl in the throat region to eliminate position error caused by drive-gear and linkage backlash. Probe travel was interrupted at each port step by the rotary valve used for wall static measurement. This port stepping resulted in at least 30 data points per probe in the throat surveys.

RESULTS AND DISCUSSION

The 3-D, mixed-compression, fixed-geometry inlet was successfully tested at $M_\infty = 6.0$. The inlet was easily started during all test runs and there was no indication of flow instability or tendency to unstart. The results obtained for the external and internal flow fields are discussed in the following sections.

External Flow Field

Flow observations.- Distinct regions of the external flow field can be seen in the schlieren photograph (fig. 4(a)). The view is the plane of symmetry ($\theta = 0^o$) at a 0^o angle of attack. The flow in the region between the conical shock wave and the cowl lip represents the spillage occurring in the off-design Mach 6 (full capture or shock on lip at Mach 10 and $\alpha = 0^o$) configuration. Some spillage of the isentropic flow field can be seen between the initial isentropic wave and the cowl lip. Design full capture of the isentropic flow occurs at Mach 8.5 at $\alpha = 0^o$. The initial internal cowl shock is indicated. Probing the boundary layer was not an objective of the test reported here, but an estimate of the thickness, at least in the $\theta = 0^o$ plane, can be obtained by scaling the schlieren picture. Centerbody boundary-layer growth (at $\alpha = 0^o$) was estimated using a modification of the method described in reference 8. Calculations were made for each instrumented radial plane (0^o, 15^o, 30^o, 45^o, and 60^o); the calculations were made assuming transition at the boundary-layer trip station. The computer program does not treat the cross flow expected from the flared elliptic portion of the centerbody, so each plane is considered as an individual case of an axisymmetric body with an adiabatic wall temperature specified for the calculation. The actual measured centerbody wall temperature

was only 74 percent of the adiabatic value. (See next section, "Wall temperatures.") A thinner boundary layer would be expected on the colder wall. The effect of angle of attack on the external flow in the vertical plane can be seen in figure 4(b). The convention defining a positive angle of attack is a counterclockwise rotation in the plane of the figure. The effect of increasing α is to increase the capture of the conical flow as indicated by the conical shock approaching the cowl lip. In references 9 and 10, it is shown that in supersonic flow around right circular cones the bow-wave angular displacement lags the body yaw or angle of attack. At a free-stream Mach number of 6.0 and a cone half-angle of 7.5°, the shock-to-cone angle-of-attack ratio is approximately 0.6. This value was used to estimate the conical bow-wave position in the $\alpha = -5^{\circ}$ configuration. The initial isentropic wave position relative to the cowl lip is nearly constant in each configuration. This consistency illustrates an advantage of the integrated engine-vehicle concept. When the engine is embedded in the shock layer of the vehicle, the inlet is essentially at a 0° angle of incidence relative to the local flow over a range of angle of attack. A comparison of schlieren photographs revealed no discernible difference in boundary-layer growth or character whether the boundary-layer trip flow was on or off; there is no evidence of flow separation in any configuration.

Wall temperatures.- Surface-temperature measurements made during the experiment were nearly uniform on a specific component of the inlet. The maximum variation in temperature on the centerbody from the spike tip to the cowl leading-edge station was ±3 percent for any given angle of attack. The following table lists the overall averages for the surface temperatures:

α, deg	Centerbody (External)	Cowl (Throat station)	Centerbody (Throat station)
	$T_w/T_{t,\infty}$	$T_w/T_{t,\infty}$	$T_w/T_{t,\infty}$
-5	0.69	0.79	0.76
0	.68	.82	.77
3	.66	.84	.77
5	.64	.82	.75
	T_w/T_{aw}	T_w/T_{aw}	T_w/T_{aw}
0	0.74	0.89	0.83

The effect of tripping the boundary layer on the wall temperature was considered negligible (less than 2-percent variation).

Wall-pressure distributions.- Figure 5(a) represents a typical longitudinal wall static-pressure distribution on the centerbody in the vertical plane ($\theta = 0^{\circ}$) at a 0° angle

of attack. This figure illustrates a small effect of boundary-layer trip flow on centerbody wall pressure. An examination of the data indicates the same small effect on the cowl wall pressures and internal flow field. Therefore, the data and results presented in the remainder of this report are taken only from the test configurations with the boundary-layer trip flow on. The delayed compression in the outboard planes of the flared elliptic portion of the centerbody downstream of the conical forebody is illustrated in the longitudinal wall-pressure plot in figure 5(b). The vertical dash on each curve marks the cowl leading-edge location, and the faired dashed curve represents the pressure distribution on the centerbody along the swept-cowl leading-edge station. Although the design goal of constant pressure along the cowl leading-edge sweep line was not achieved, the slight decrease of pressure in the outboard planes had a negligible effect on the internal flow at the throat station. The effect of the angle of attack on the centerbody surface-pressure distribution in different radial planes can be seen in figures 5(c) to 5(g). The expected pressure increase as a result of a positive angle-of-attack increase is most pronounced in the vertical plane (windward side); the pressure increase is affected to a lesser extent in the outboard planes.

Internal Flow Field

Shock diagrams.- Two-dimensional (2-D) shock patterns were analytically generated for the inlet internal geometry with a 2-D shock pattern for each instrumented radial plane. The results are shown in figure 6. The initial flow conditions (Mach number, pressure, and flow angle) in Bay 1 of each diagram were assumed to be an average of the cowl-lip station value and the centerbody inviscid wall value at the capture station. The initial wedge on the inner cowl surface is 2° upward relative to the horizontal center line in each radial plane and extends for a constant length of 5.08 cm from the leading edge. This wedge is followed by a horizontal surface and then by a 10° expansion. A cancellation of the cowl leading-edge shock on the centerbody shoulder located at the throat station was intended to occur at $M_{\infty} = 6$, but the impingement and reflection can be seen slightly ahead of this position. Cancellation of the internal shock waves at higher free-stream Mach numbers would be achieved by instream fuel injectors. The fuel-injector concept is discussed in reference 3. An examination of the diagrams indicates a greater number of shock intersections and reflections ahead of the centerbody shoulder in the outboard planes. Flow parameters obtained from these diagrams are tabulated in figure 6 and are used for comparison with survey data discussed in the "Survey data" section. The internal-flow analysis was made only for the case of a 0° angle of attack and the leading edge was assumed to be sharp. Sidewall effects in the $\theta = 60^{\circ}$ plane are not included in the analysis. Although this analysis does not account for 3-D effects of the swept flow field or of the internal-flow boundary layer, sufficient information was obtained to predict pressure transducer ranges and values of throat-flow parameters; such values compare favorably with measured values.

Internal wall pressures.- Pressure measurements for the internal surfaces are given in figures 7(a) to 7(d). The internal wall pressures presented in this section were obtained without survey rakes installed. Figure 7(a) shows the pressure distribution along the cowl inner surface at a 0° angle of attack. The wall pressure is nondimensionalized by the free-stream static pressure and the longitudinal distance is measured relative to the cowl leading edge in the respective radial plane. The dashed-line step distribution is determined from the calculated 2-D shock patterns shown in figure 6. In the plane of symmetry ($\theta = 0^{\circ}$) the 2-D analysis should be reasonably valid. Quantitative differences can be noted between the data results and the calculated values, but distinct flow regions of the shock patterns are clearly evident. In the region immediately downstream of the initial shock (Bay 2), the pressure is essentially constant; the second shock pressure rise to Bay 3 follows. The abrupt pressure rise at $X = 7.62$ cm represents the reflection from the centerbody of the initial cowl shock onto the cowl surface at the throat. The outboard planes show fair agreement with theory except in the 30° and 45° planes. Here again it should be emphasized that the shock analysis assumes a sharp cowl leading edge and a zero-radius wedge at the $X = 5.08$-cm station; the analysis does not account for internal boundary-layer growth or swept flow displacement of the shock waves and cross flow. A discussion of the effects of leading-edge bluntness on inlet performance is given in reference 2. The cowl wall-pressure distributions at a varied angle of attack are shown in figure 7(b). The trends are generally the same as for the distributions at $\alpha = 0^{\circ}$, but with pressure levels that increase with a larger angle of attack.

Centerbody wall internal-pressure variation in the instrumented radial planes for $\alpha = 0^{\circ}$ is shown in figure 7(c). The decrease in pressure at $X = 7.62$ cm for $\theta = 0^{\circ}$ and $\theta = 15^{\circ}$ is in the expansion region immediately downstream of the shoulder at the beginning of the throat section. The pressure rise associated with the shock reflections and intersections can be seen in the outboard planes (30°, 45°, and 60°). The sidewall internal-pressure distributions are seen in figure 7(d) over the angle-of-attack range. The left sidewall ($\theta = 60^{\circ}$) indicates good flow alinement with a moderate pressure rise at low angles of attack and at the forward positions on the wall. Further downstream the pressure rises rapidly and the distortions caused by corner flow become more pronounced.

Survey data.- Representative test data from survey probe measurements have been selected and are presented in figures 8 and 9. The upper end points ($Z = 1.0$) for the pressure profiles are determined from wall static-pressure measurements. In the vertical plane ($\theta = 0^{\circ}$) the wall-pressure orifices are in the same plane as the center probe (Probe 5) of Rake 1. The end points for this case are indicated as data by symbols. All other end points are interpolated values from adjacent orifices. In figure 8(a) pitot-pressure profiles are shown at the vertical center-line position (Rake 1) at a 0° angle of attack. This survey rake has nine probes which are symmetric about the vertical plane ($\theta = 0^{\circ}$) and are swept to follow the throat line. The plots are made with each correspond-

ing set of probes on either side of the vertical center line; with the exception of Probes 3 and 7 the measurements show excellent flow-field symmetry. The pitot-pressure profiles in figure 8(b) are for the center probe of each rake at a 0° angle of attack. Quantitatively, the profile of Rake 1 agrees well with the flow picture of figure 6 over 65 percent of the vertical probe travel. The measured pressures at $Z = 0.45$ and $Z = 0.60$ agree well with the theoretical values in Bays 4 and 3, respectively, of the shock pattern for $\theta = 0^{\circ}$. Profiles in the outboard planes are similar in shape with the shock positions less pronounced in the Rake 3 plane. Pitot-pressure profile variations as a result of angle of attack are shown in figure 8(c). A similarity in profile shapes can be seen in the first three planes with a trend of increasing pressure corresponding with the angle of attack. The profiles of the most outboard plane are similar in shape but do not display any specific order of variation with the angle of attack. Even though the left sidewall center-line pressures (fig. 7(d)) indicated good flow alinement, the possibility of lateral shocks from the cowl-sidewall and centerbody-sidewall junctions is not excluded.

Static-pressure survey data are presented in figure 9 using the same format as that of the pitot data. With the exception of the Probe 1 and 9 profiles in figure 9(a), the static-pressure measurements also indicate good flow symmetry. The static-pressure profiles of the center probe for each rake at a 0° angle of attack are shown in figure 9(b). The effect of the angle of attack on static pressure is shown in figure 9(c) and, in general, indicates an increase in pressure with an increased α. Like the pitot-pressure profiles in the outboard plane ($\theta = 52.5^{\circ}$) the static-pressure distribution shows no specific trend of variation with the angle of attack.

Pitot survey data showed good agreement with the shock diagrams of figure 6, while static survey data do not agree well except at the cowl and centerbody walls. Measurements made in the throat region of an inlet are complicated by highly confined space, internal shock-wave interference, and probe shock-wave reflection near walls. The internal flow picture of figure 6 illustrates some of these effects. For instance, in the $\theta = 0^{\circ}$ plane the probe tip position at the start of a survey is at the shoulder on the centerbody at the throat station, while the orifice on the probe is downstream in a low-pressure expanded flow region. As the probe moves upward the orifice is swept by the expansion fan while the tip is intercepting the inlet internal shocks. Tabulated results of the theoretical shock-wave analysis (fig. 6) show flow angles relative to the horizontal static probes as high as 10.66°. The accuracy of pitot-tube measurements is good up to a flow misalinement of 10°, but conventional static-pressure probe errors are large at flow angles of this magnitude. A comparison of the measured and calculated static-pressure profiles show measured values to be generally low with errors as large as 50 percent. The possibility of erroneous pitot-pressure measurements exists; however, static-pressure errors are considered more significant in data reduction. Therefore, the pitot-pressure data are considered the most accurate and, in the event of a computed pressure recovery exceeding 100 percent,

the static pressure is considered to be in error. Using the survey data, a Mach number and a total pressure are calculated. If this total pressure exceeds a previously computer-input limiting value, the limiting value is used to compute a new value of static pressure. All parameters are then determined with the corrected value. The limiting pressure recovery used was a value of 91 percent of the free-stream total pressure. This recovery is determined by the inviscid value at the capture station and by additional internal shock losses.

Contour plots.- Pitot- and static-pressure survey data were reduced by a computer program featuring a curve-fitting interpolation procedure capable of expanding the data into a network of grid points covering the throat flow area. From the input pressure data, the program computes Mach number, total pressure recovery, and mass flow per unit area for each grid point. Contour plots of each parameter are also plotted by the program; numerical integration over the grid yields mass weighted averages of the flow parameters.

Figures 10(a) and 10(b) contain contours of constant pitot pressure. For the purpose of clarity the ratio of survey height to rake width is not drawn to scale in the plots. Figure 10(a) shows the pressure distribution at each of the four rake stations for the 0° angle-of-attack configuration. The plots indicate a uniform distribution over a large percentage of the throat flow area with an overall average pressure level of approximately 200. The contours about the vertical center line (Rake 1 data) shown in figure 10(b) illustrate the relative insensitivity of the internal flow distribution to the angle of attack. While the pressure level increases with α, the distribution remains uniform. This uniformity is also reflected in the static-pressure distribution shown in figures 10(c) and 10(d). The contours in these figures contain large numbers (as high as 50 percent of the total) of grid point values computed using the limiting pressure-recovery correction method discussed in the "Survey data" section. The distribution variation of static pressure with the angle of attack (fig. 10(d)) is similar to that of pitot pressure.

Two important parameters used in determining scramjet performance from a thermodynamic cycle analysis are the average Mach number and the total pressure recovery at the end of the inlet compression process. Contour maps of these parameters are presented in figures 10(e) to 10(h). In the $\alpha = 0^{\circ}$ configuration (fig. 10(e)), Mach number distribution and level are uniform over a large percentage of the area at each survey station. The effect of the angle of attack on Mach number in the $\theta = 0^{\circ}$ plane is shown in figure 10(f). Pressure-recovery plots in figures 10(g) and 10(h) indicate relatively large areas in which values calculated from measured static pressures equaled or exceeded the limiting recovery of 91 percent.

Integrated flow parameters.- As mentioned earlier, the data processing computer program numerically integrates the survey station flow parameters over the grid area. The results of this integration include mass flow per unit area, mass weighted Mach

number, and total pressure recovery. Throat Mach number is shown in figure 11(a) as a function of radial plane for a 0° angle of attack. The symbols are average values at each rake position, and the dashed curve represents the theoretical inviscid values calculated from the 2-D shock diagrams in figure 6. The overall average of the theoretical values is approximately 6 percent higher than the Mach number calculated from flow measurements. The range of limiting total pressure recovery used in the data reduction was varied (0.91, 0.81, and 0.71) and the effect on Mach number level was found to be a variation of 6 percent. The important features of these results are the Mach number level and its uniformity over the entire lateral span of the swept throat. The level of the parameter is approximately the correct value for efficient combustor design. This value would be further reduced by a geometric contraction which is produced by the fuel injectors until an optimum combustor entrance Mach number of approximately 40 percent of the flight Mach number is reached (ref. 11). Figure 11(b) shows an arithmetic average of the four survey rake Mach numbers over the angle-of-attack range. Throat Mach number variation relative to the $\alpha = 0^{\circ}$ value was 5 percent higher at $\alpha = 3^{\circ}$ and 3 percent lower at $\alpha = 5^{\circ}$.

Mass averaged total pressure recovery at the throat station is shown in figure 12 for the three limiting values of recovery indicated as $\eta_{D,max}$. In the 0° angle-of-attack case, the dashed curve is from the shock diagrams. Of the three values of limiting recovery used in data reduction, 91 percent is considered the most realistic number. The results based on 0.81 and 0.71 were calculated to determine the effect of limiting recovery on performance parameters. As stated previously, the effect this value has on Mach number was found to be small. While the effect on mass weighted recovery appears to be large (a variation of 19 percent), the corresponding inlet adiabatic kinetic-energy efficiency is changed by a negligible amount (less than 1 percent). The average theoretical value for $\alpha = 0^{\circ}$ ($\eta_D = 0.79$) was 7 percent higher than the average of the four survey stations ($\eta_D = 0.74$) for the inviscid limiting case of $\eta_{D,max} = 0.91$. The sharp decrease in recovery in the outboard plane ($\theta = 52.5^{\circ}$) is attributed to boundary-layer losses. After the assembly of the model it was discovered that the boundary-layer bleed passage gradually trails off to zero area at the sidewall. This loss is produced by the combination of large quantities of boundary-layer buildup in this plane along the entire length of centerbody and the outflow produced by sweep. A contribution to pressure loss can also be made by corner flow and shocks from the left sidewall. This condition was discussed earlier as a possible cause of distortion of pitot-pressure survey profiles in the $\theta = 52.5^{\circ}$ plane. The average level of recovery increases with the angle of attack, and the plots in figure 12(a) show the gain to be largest in the $\theta = 0^{\circ}$ and $\theta = 37.5^{\circ}$ planes. Figure 12(b) shows this recovery increase more clearly. In the case of $\eta_{D,max} = 0.91$, $\theta = 0^{\circ}$ values increase 14 percent from 0.70 to 0.80 and $\theta = 37.5^{\circ}$ results have a gain of 12.5 percent from 0.80 to 0.90. Average values at the other two stations remain relatively con-

stant. Finally, an arithmetic average of the recovery over the throat area for each angle of attack is presented in figure 12(c). The average of these four values is 78 percent.

Performance parameters.- Measured inlet throat flow parameters and averaged values of them are used in conjunction with the geometry to calculate quantities that define overall inlet performance and desirable features of the throat conditions. The Mach number, the total pressure recovery level, and the uniform distribution have been discussed. The average Mach number and recovery levels were used to obtain the following performance parameters: static-pressure compression ratio, capture-area ratio, and aerodynamic-contraction ratio. Also, an inlet kinetic-energy efficiency can be calculated from the recovery and free-stream Mach number. For the average $\bar{\eta}_D = 0.78$ obtained from figure 12(c), the corresponding adiabatic kinetic-energy efficiency η_{KE} is 99 percent. Both of these values are high relative to many axisymmetric inlets.

The average static pressure at the throat was determined from M_T and η_D and is shown in figure 13(a). An arithmetic average of the survey station values for each angle of attack is shown in figure 13(b). The dashed curve represents the compression ratio obtained if reference conditions are at the beginning of the isentropic compression. This reference condition was included to provide a means of comparing this inlet performance with inlets which are not embedded in the vehicle shock layer. An average (M = 5.38) of the surface and wave Mach number in the conical field was used as the reference condition.

Another indicator of engine performance level is the capture-area ratio value and variation over the operating range. The capture-area ratio is defined as

$$\left(\frac{A}{A_{capture}}\right)_{ref} = \frac{\dot{m}_T}{(\dot{m}/A)_{ref}}\left(\frac{1}{A_{capture}}\right)_{ref}$$

where A is the area of a streamtube required to pass the captured mass flow at reference conditions. If the inlet is operating below design Mach number, the capture-area ratio and hence the mass-flow ratio are less than unity. In order to evaluate this parameter, the boundary-layer bleed flow must be added to the measured throat flow to evaluate the capture mass flow. The centerbody boundary-layer program analysis was used to determine the mass flow per unit area at the scoop station; full capture of the bleed passage was assumed. The nominal value of the bleed flow over the range of α was 4 percent of $\dot{m}_{capture}$. For a 0^o angle of attack, the throat mass flow calculated from the experimental data (0.89 kg/sec) was approximately 3 percent higher than the predicted value (0.87 kg/sec). The variation of capture-area ratio is shown in figure 14. The trend of increasing capture with α is verified by an observation of figure 4(b). The spillage of the conical flow decreases as α increases. The level of capture over this range (-5^o to 5^o) is adequate (ref. 2) for the design vehicle performance requirements at

$M_\infty = 6$. When referenced to the isentropic field, this parameter indicates 86 percent at $\alpha = -5^\circ$ and full capture from $\alpha = 0^\circ$ to $\alpha = 5^\circ$; however, full capture design conditions for this flow were $M_\infty = 8.5$ and $\alpha = 0^\circ$. Some spillage of the isentropic flow is noted in figure 4(b) for all values of α. The last performance indicator, the aerodynamic-contraction ratio, is shown in figure 15. This ratio is given by

$$\left(\frac{A}{A_T}\right)_{ref} = \frac{(A/A^*)_{ref}}{(A/A^*)_T}(\eta_D)$$

where A/A^* is the streamtube critical-area ratio. These values are given primarily so that comparisons can be made with inlets having undefinable geometric contraction. Additional compression by the fuel injectors and by the thermal-compression process would increase these values.

CONCLUDING REMARKS

The experimental results of a three-dimensional, fixed-geometry, mixed-compression inlet investigation have been presented. The tests were conducted at a free-stream Mach number of 6.0, a Reynolds number of 1.55×10^7 per meter, and stagnation conditions of 20 atmospheres and 500 K. The following observations are made in reference to the experimental results of this investigation:

1. No difficulty was encountered in the starting process of the inlet. After start there was no indication of flow instability or tendency to unstart.

2. The inlet performance derived from pressure measurements was consistently high over the range of angle of attack tested. An overall average total pressure recovery of 78 percent and the corresponding adiabatic kinetic-energy efficiency of 99 percent were obtained over the range of angle of attack. Also, the captured mass flow was sufficient for the design engine performance requirements at a free-stream Mach number of 6.0.

3. The flow distribution was relatively uniform at the inlet throat.

4. Mach number and pressure levels at the inlet throat are approximately the correct value for efficient combustor design.

5. For the 0° angle-of-attack configuration, the predicted throat flow parameters relative to the values calculated from measurements were as follows: total pressure recovery was 7 percent higher, Mach number was 6 percent higher, and throat mass flow was 3 percent lower.

6. The experiment verified that the concept of utilizing a swept compression field to meet the starting requirements of fixed geometry can produce high performance inlets.

Langley Research Center
National Aeronautics and Space Administration
Hampton, Va. 23665
June 17, 1975

REFERENCES

1. Henry, J. R.; and McLellan, C. H.: Air-Breathing Launch Vehicle for Earth-Orbit Shuttle – New Technology and Development Approach. J. Aircraft, vol. 8, no. 5, May 1971, pp. 381-38 .

2. Agnone, Anthony Michael: Design and Theoretical Performance Estimate of a Three Dimensional Integrated Scramjet Engine. Ph. D. Thesis, New York Univ., 1973.

3. Andrews, Earl H., Jr.; Agnone, Anthony M.; and Pinckney, S. Z.: Experimental and Analytical Study of an Inlet Forebody for an Airframe-Integrated Scramjet Concept. NASA TM X-3158, 1975.

4. Lehrhaupt, Harry: Supersonic Flow Calculations for a Cone With an Elliptic Flare. NASA CR-112301, 1970.

5. Scheuing, Richard Albert: Three Dimensional Supersonic Flow Over a Smooth Body With Shock-Producing Protuberance. Ph. D. Thesis, New York Univ., 1971.

6. Miyazaiwa, Masafumi: A New Technique for Inducing a Turbulent Boundary Layer in a Supersonic Flow. NASA CR-132554, 1974.

7. Goldberg, Theodore J.; and Hefner, Jerry N. (With appendix by James C. Emery): Starting Phenomena for Hypersonic Inlets With Thick Turbulent Boundary Layers at Mach 6. NASA TN D-6280, 1971.

8. Pinckney, S. Z.: Method for Predicting Compressible Turbulent Boundary Layers in Adverse Pressure Gradients. NASA TM X-2302, 1971.

9. Staff of Computing Section Center of Analyses (Zdenek Kopal, Director): Tables of Supersonic Flow Around Cones of Large Yaw. Tech. Rep. No. 5, Mass. Inst. Tech., 1949.

10. Sims, Joseph L.: Tables for Supersonic Flow Around Right Circular Cones at Small Angle of Attack. NASA SP-3007, 1964.

11. Weber, Richard J.; and MacKay, John S.: An Analysis of Ramjet Engines Using Supersonic Combustion. NACA TN 4386, 1958.

L-71-5415

Figure 1.- Vehicle-engine integration concept.

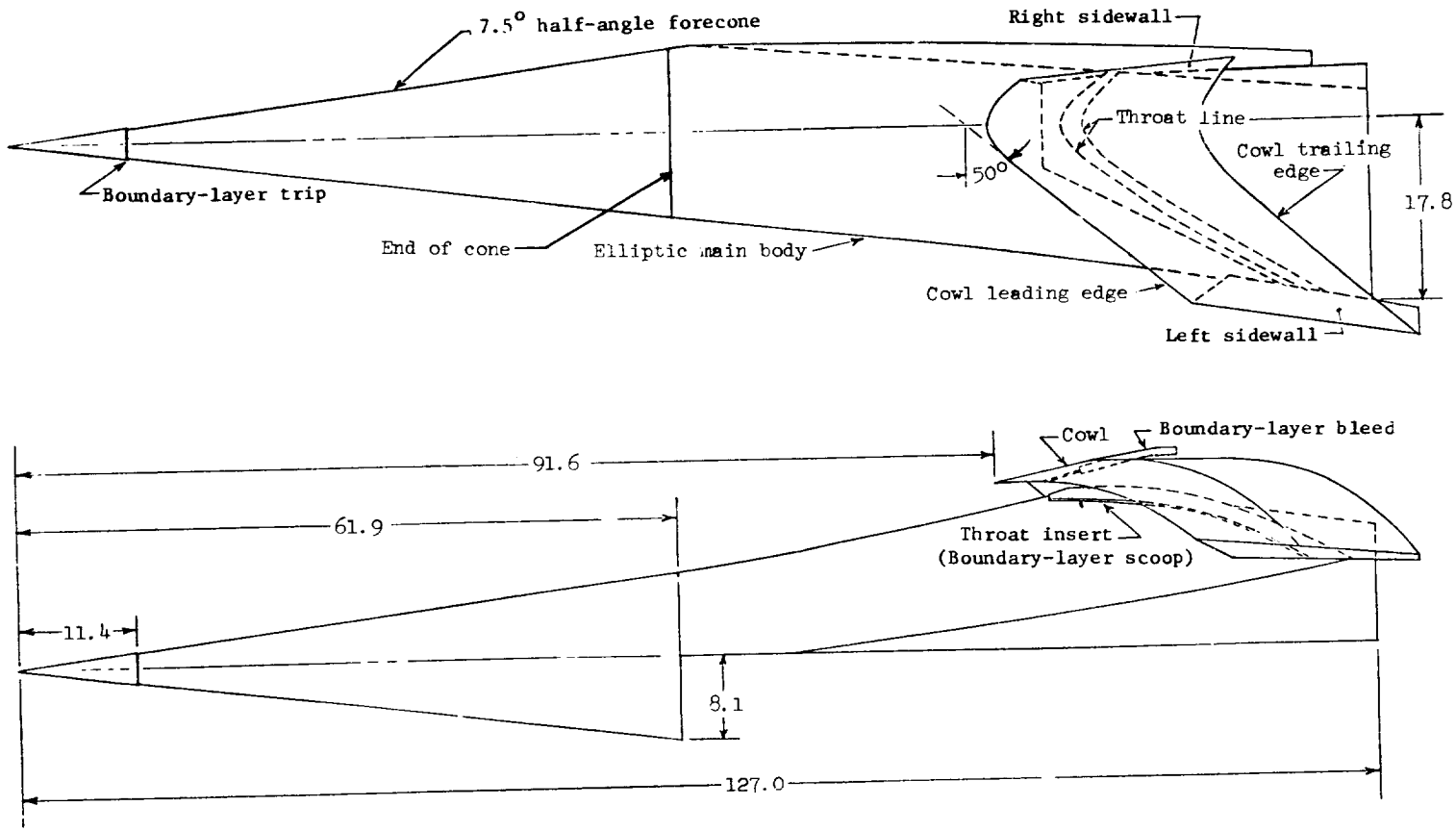

(a) Model sketch. Dimensions are in centimeters.

Figure 2.- Model description.

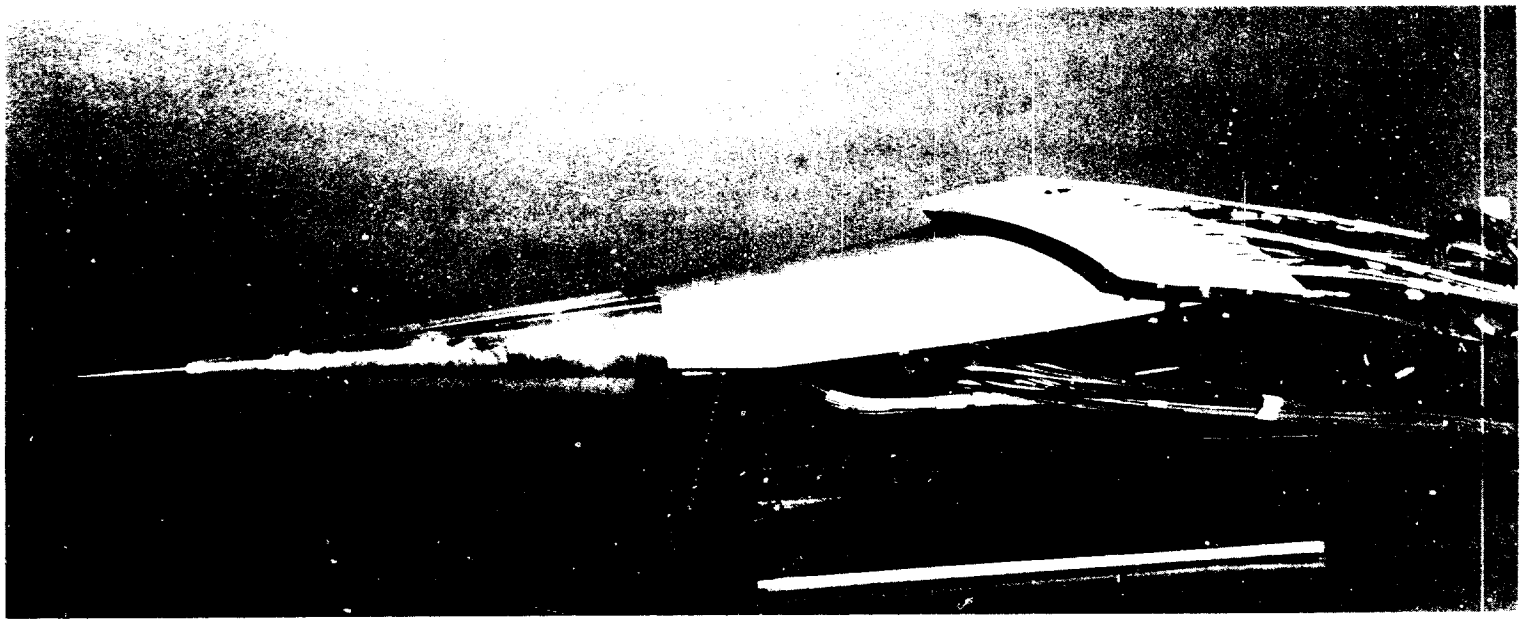

L-72-7424

(b) Photograph of model.

Figure 2.- Continued.

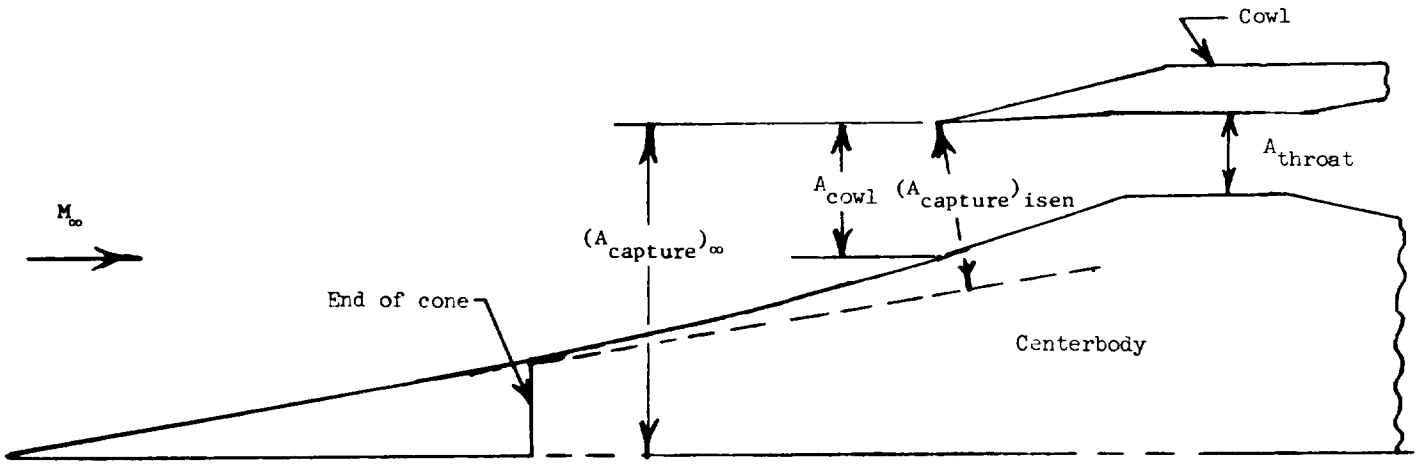

$$\text{External contraction ratio} = \frac{(A_{capture})_\infty}{A_{cowl}}$$

$$\text{Total contraction ratio} = \frac{(A_{capture})_\infty}{A_{throat}}$$

$$\text{Internal contraction ratio} = \frac{A_{cowl}}{A_{throat}}$$

(c) Geometric contraction ratio definition.

Figure 2.- Continued.

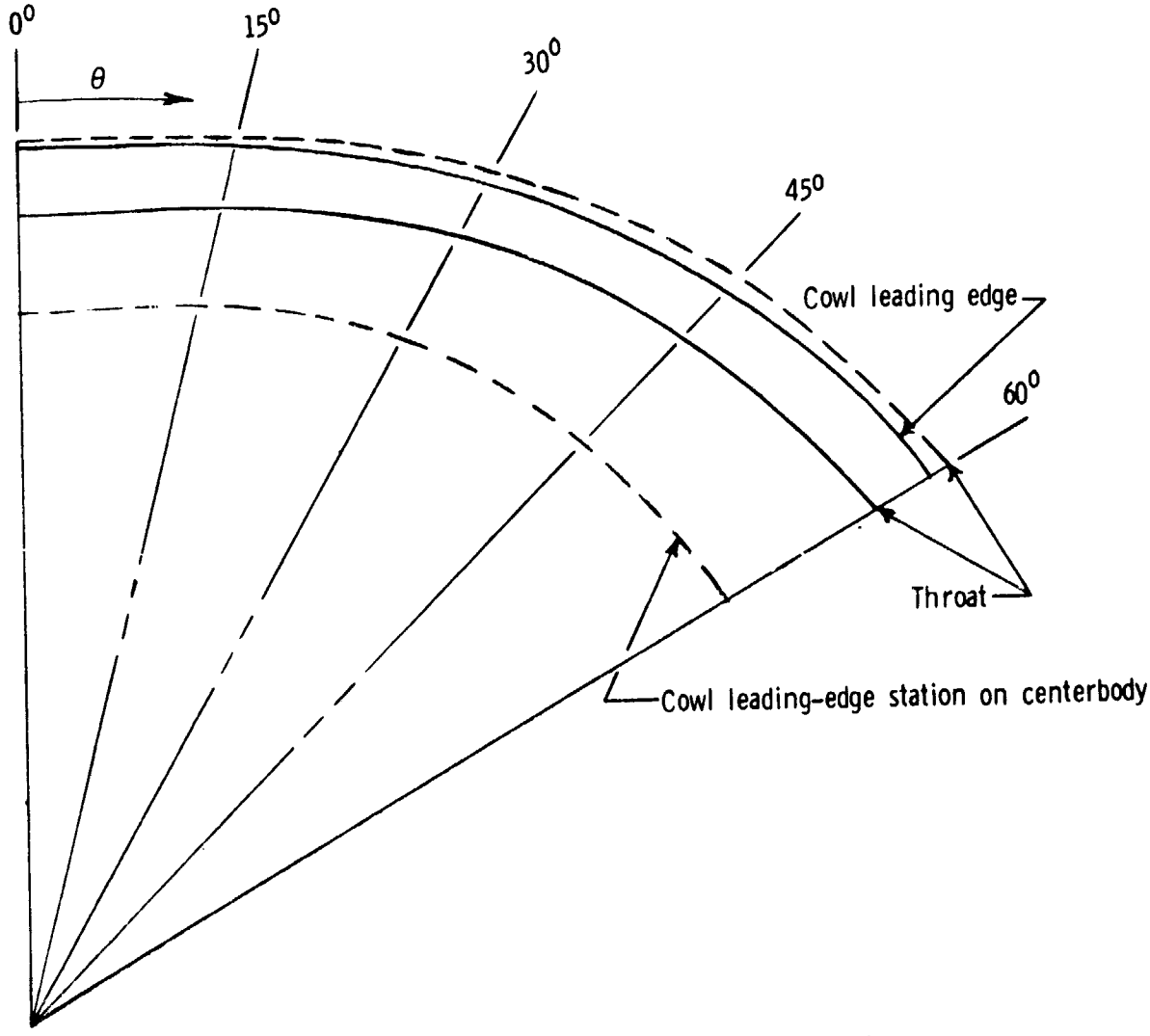

(d) Radial plane angle convention (frontal view).

Figure 2.- Concluded.

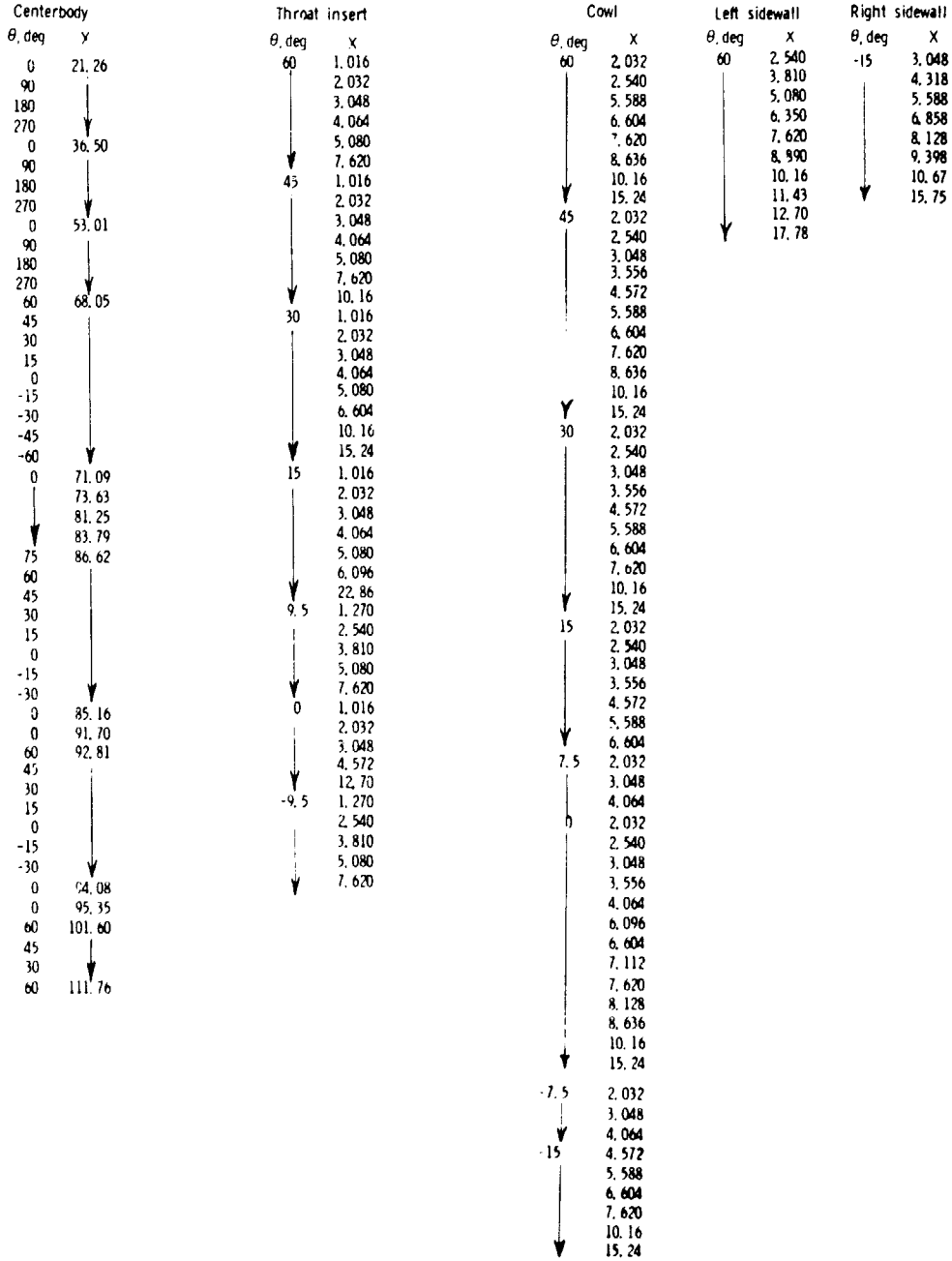

(a) Wall static-pressure orifice locations.

Figure 3.- Instrumentation location.

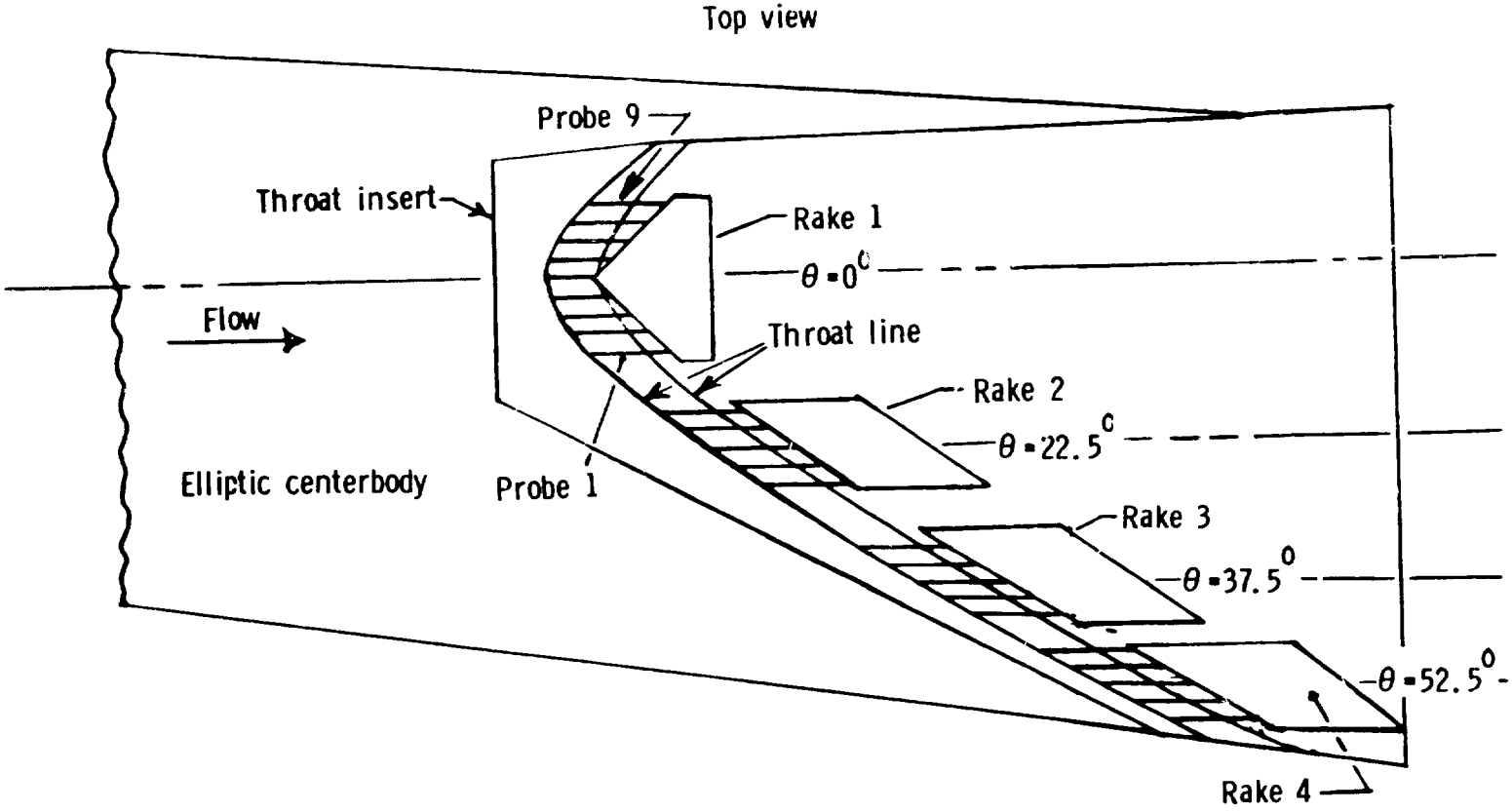

(b) Survey-rake orientation.

Figure 3.- Continued.

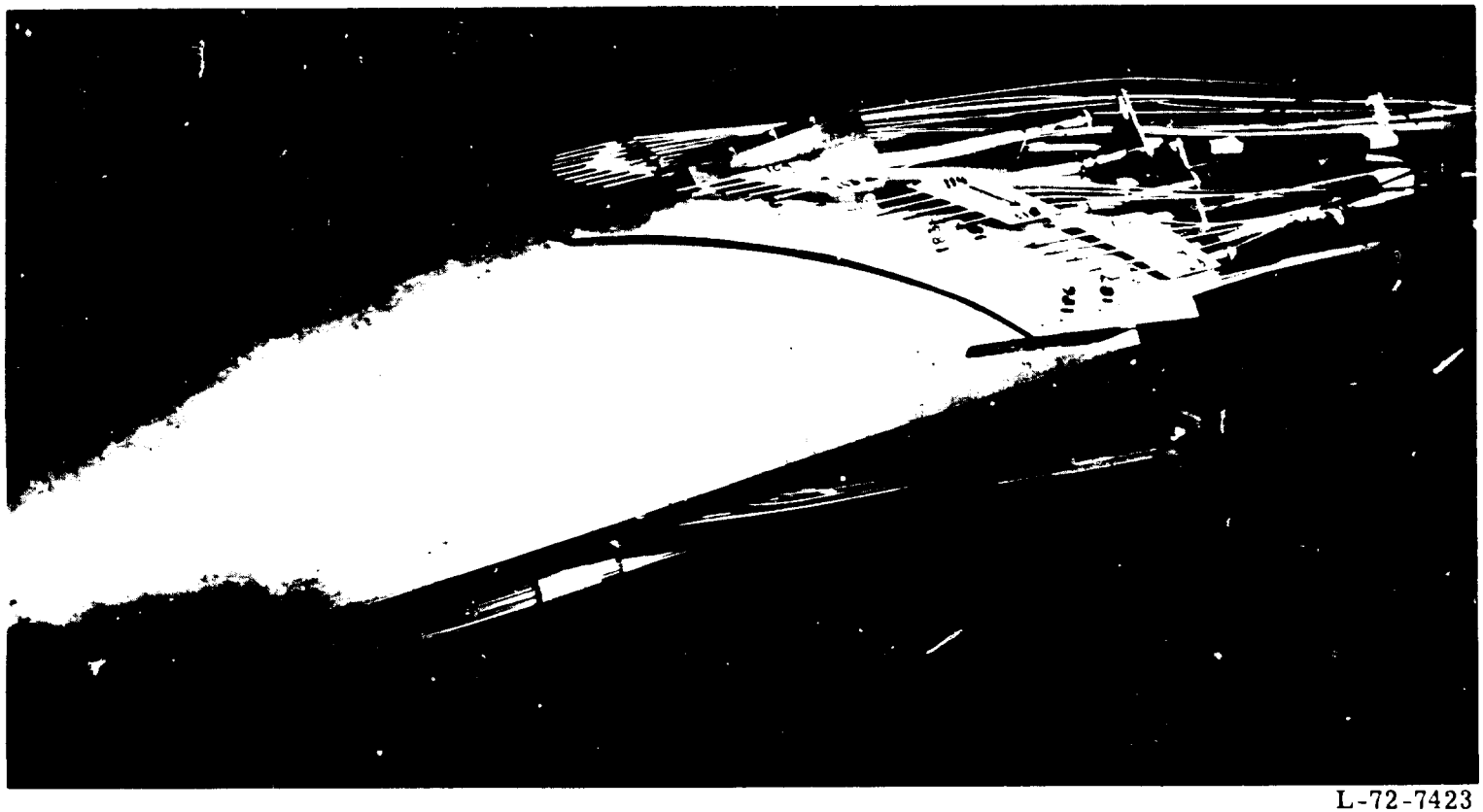

L-72-7423

(c) Photograph of survey rake installation.

Figure 3.- Concluded.

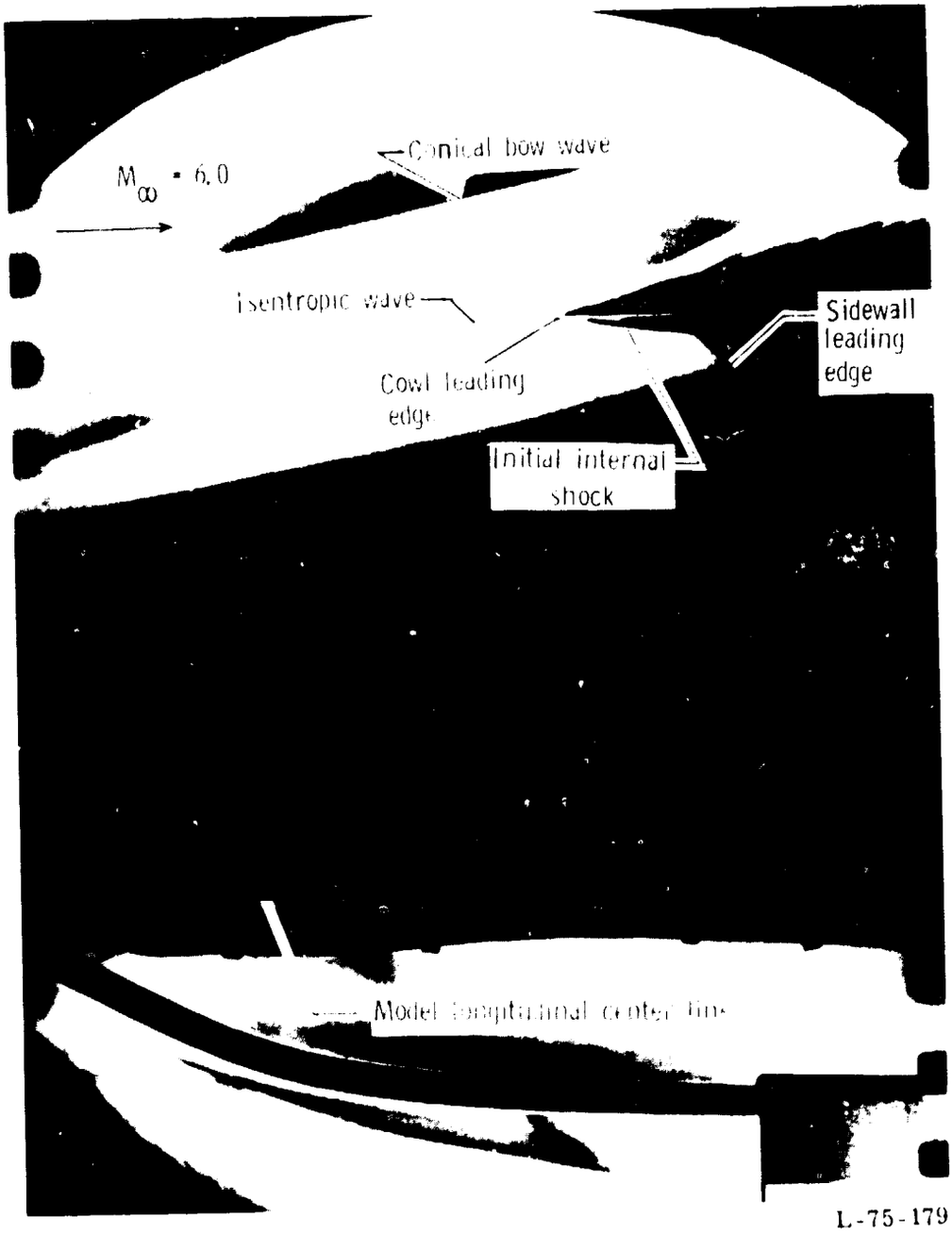

(a) $\alpha = 0^\circ$; $\alpha = 0^\circ$.

Figure 4.- Schlieren photographs.

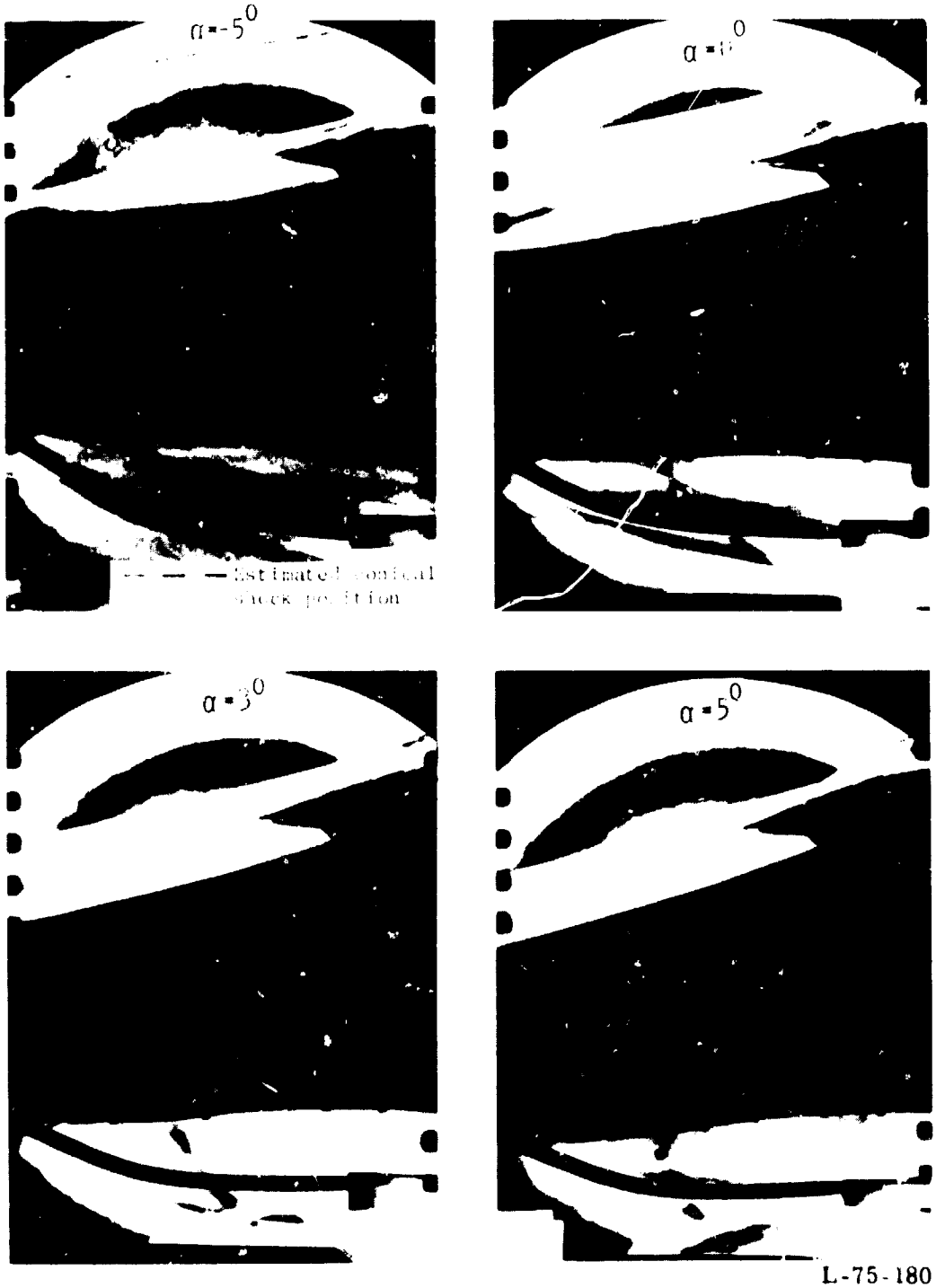

(b) Angle of attack varied.

Figure 4.- Concluded.

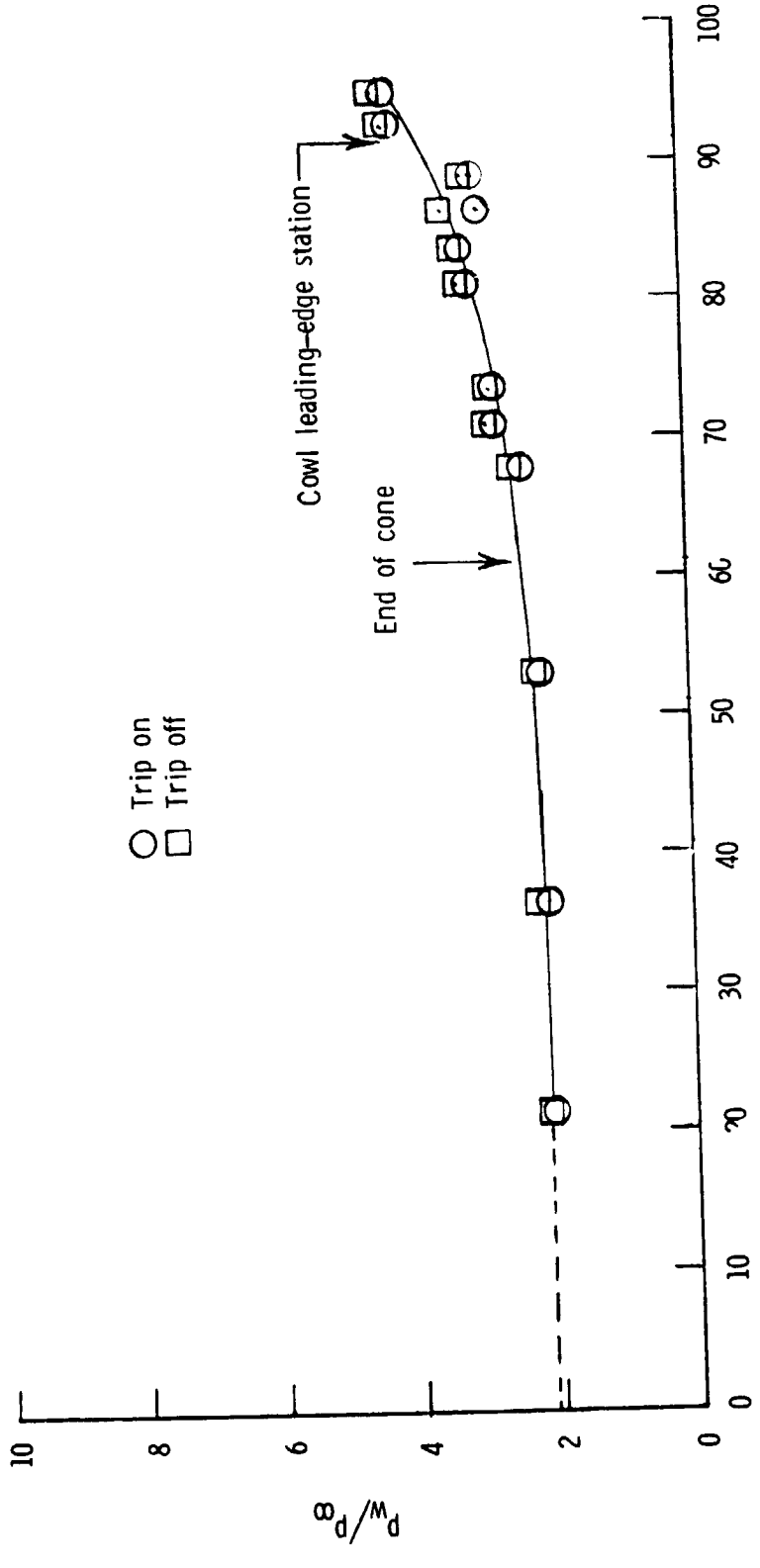

(a) Boundary-layer trip effect; $\theta = 0^o$; $\alpha = 0^o$.

Figure 5.- Centerbody longitudinal wall-pressure distribution.

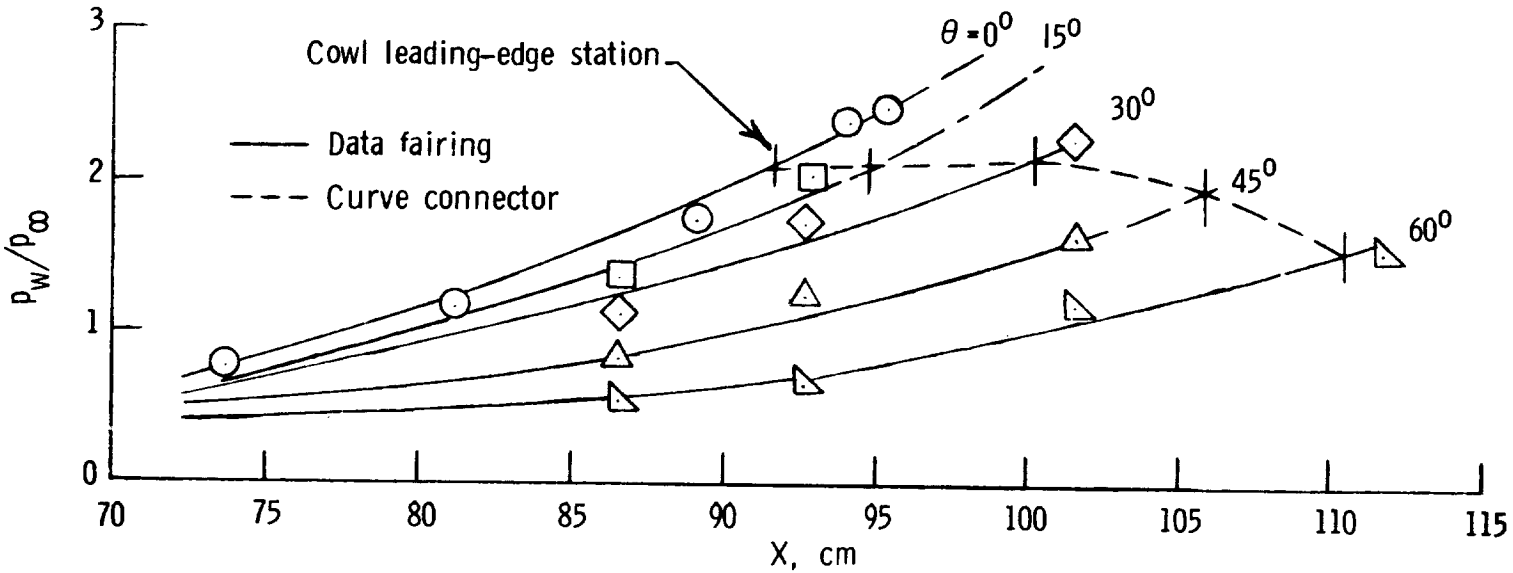

(b) $\alpha = 0^{\circ}$.

Figure 5.- Continued.

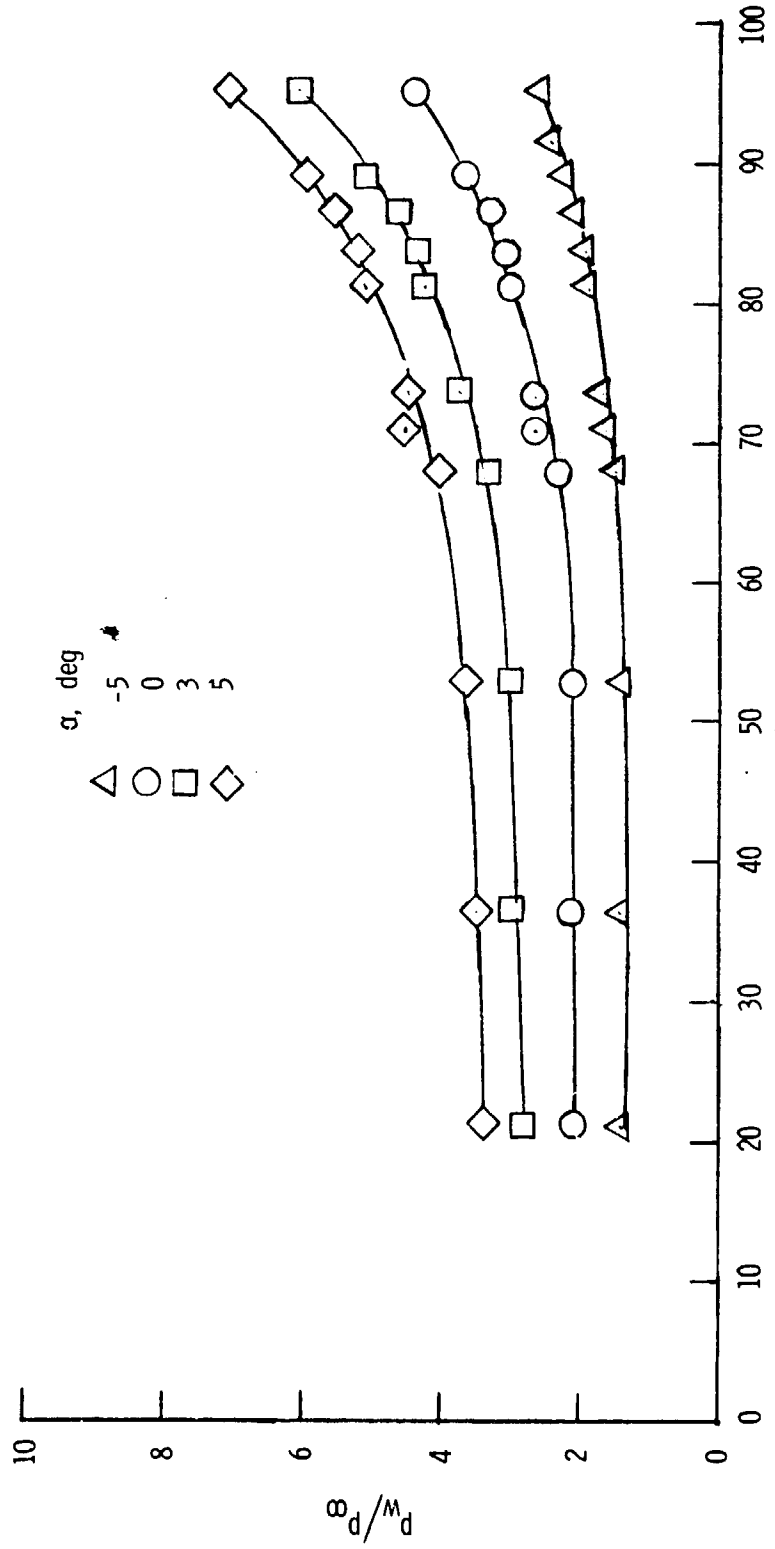

(c) $\theta = 0^o$.

Figure 5.- Continued.

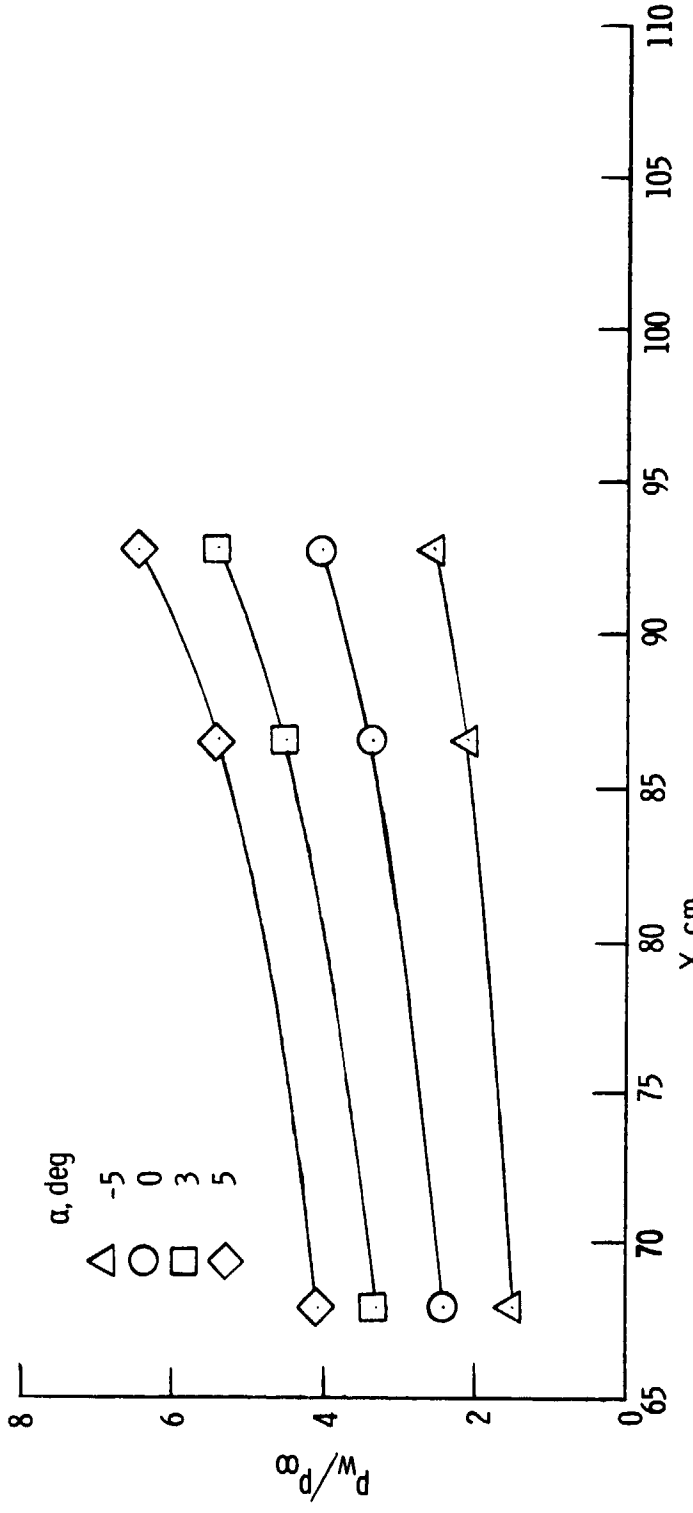

(d) $\theta = 15^{\circ}$.

Figure 5.- Continued.

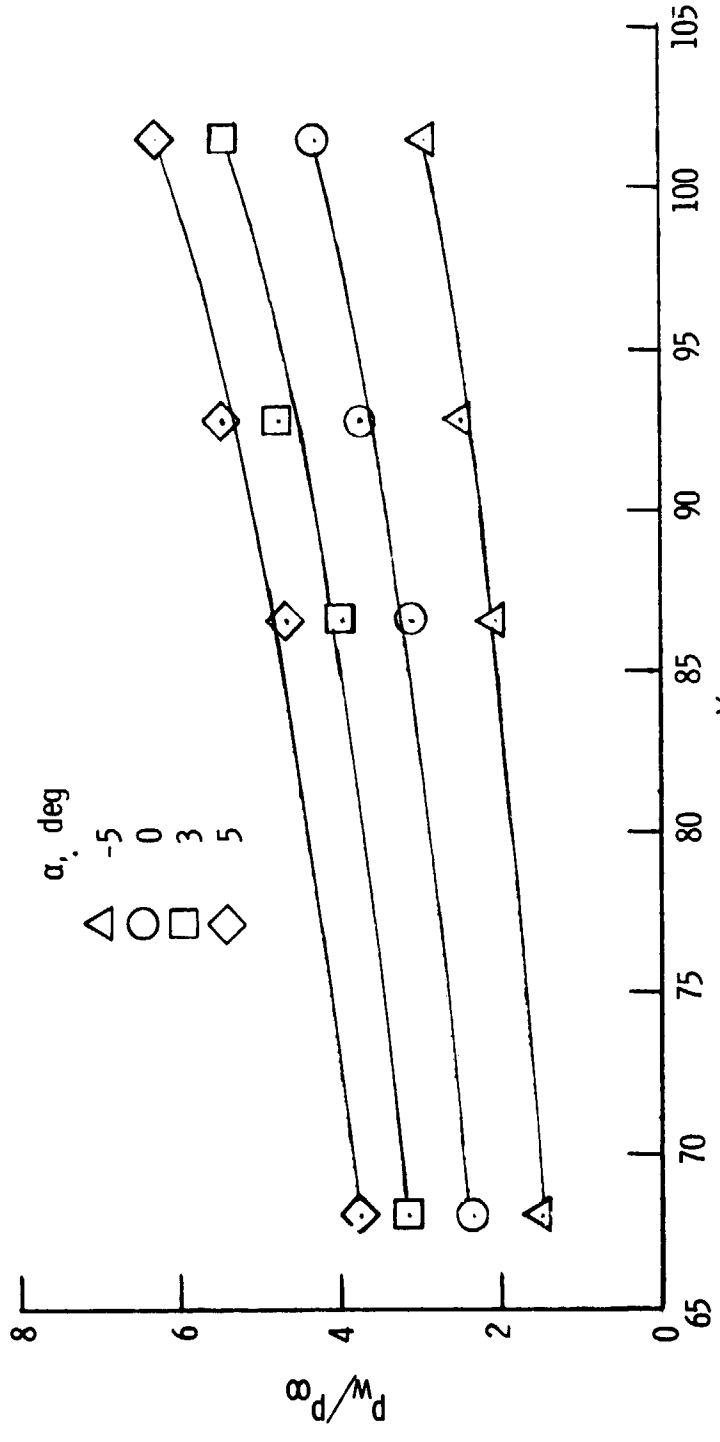

(e) $\theta = 30^{\circ}$.

Figure 5.- Continued.

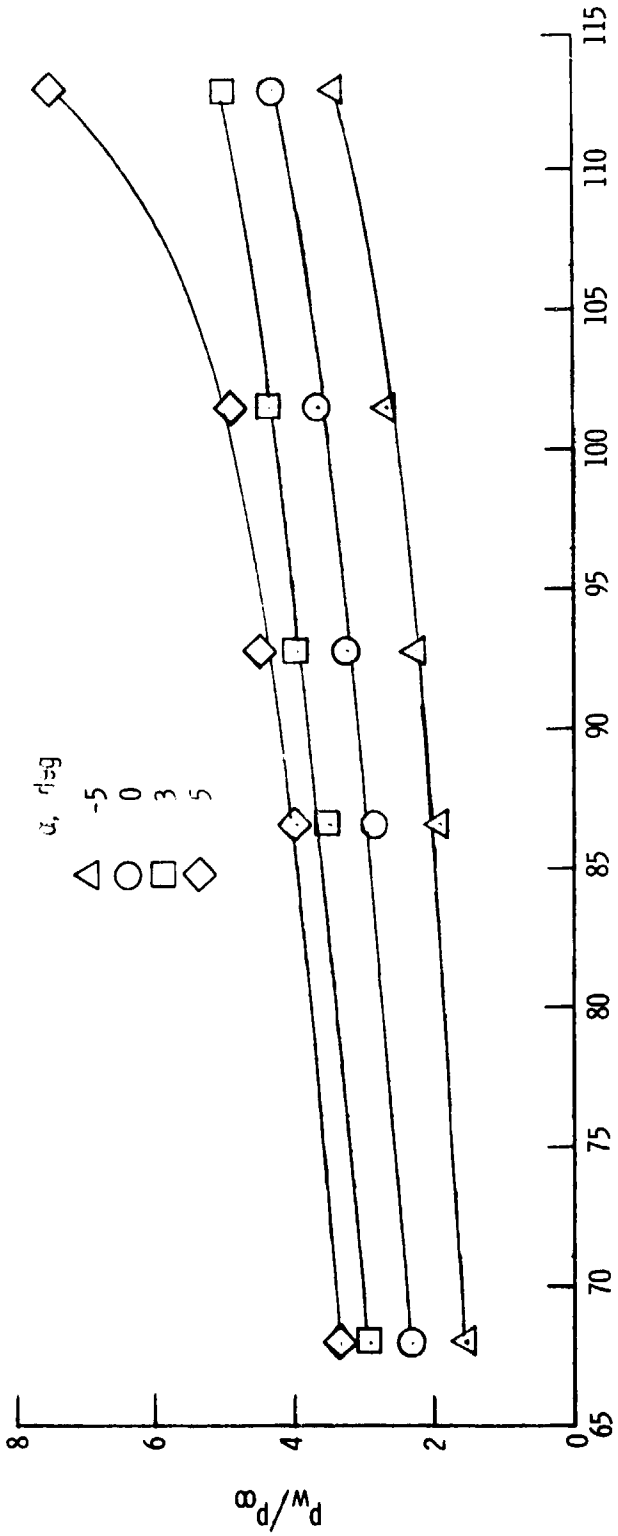

(f) $\theta = 45^\circ$.

Figure 5.- Continued.

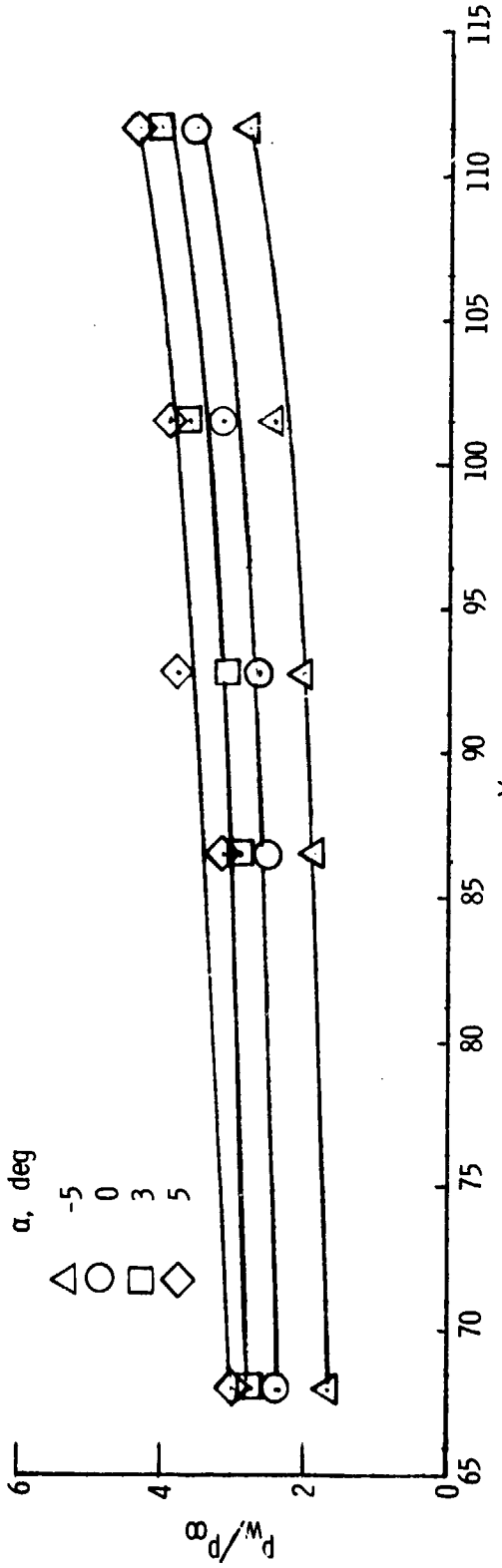

(g) $\theta = 60^{o}$.

Figure 5. - Concluded.

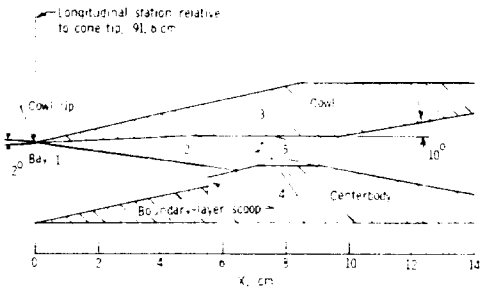

(a) $\theta = 0^{O}$.

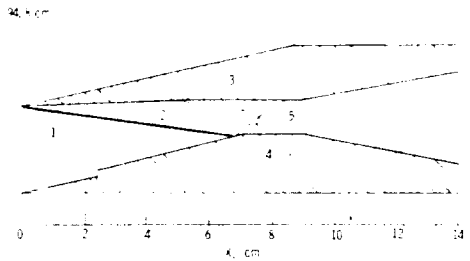

(b) $\theta = 15^{O}$.

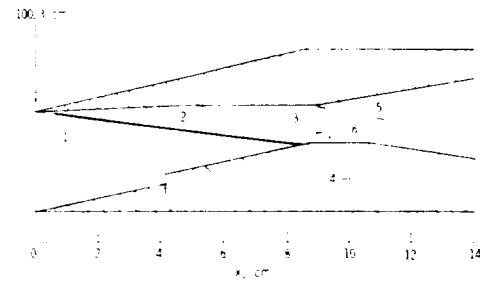

(c) $\theta = 30^{O}$.

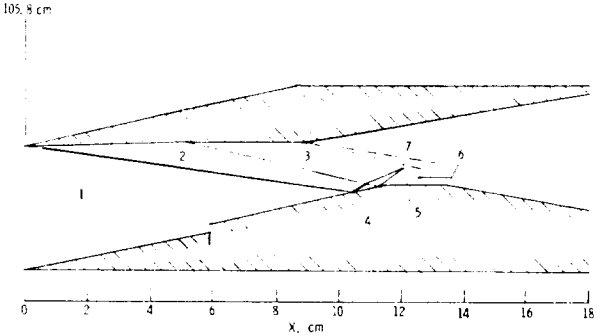

(d) $\theta = 45^{O}$.

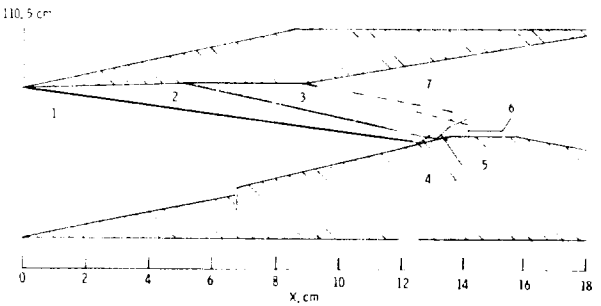

(e) $\theta = 60^{O}$.

θ, deg	Bay	Mach No.	Flow angle, deg	$p_t/p_{t,\infty}$	θ, deg	Bay	Mach No.	Flow angle, deg	$p_t/p_{t,\infty}$
0	1	4.895	10.59	0.986	45	1	4.992	9.26	0.986
	2	4.066	2.00	.903		2	4.261	2.00	.929
	3	3.914	0.00	.902		3	4.096	0.00	.928
	4	3.437	10.59	.856		4	3.687	9.26	.894
	5	3.318	8.59	.855		5	3.558	7.28	.893
15	1	4.876	10.66	.986		6	3.433	9.26	.891
	2	4.041	2.00	.907		7	5.012	10.00	.928
	3	3.890	0.00	.901	60	1	4.998	8.97	.986
	4	3.411	0.00	.864		2	4.298	2.00	.936
	5	3.303	0.00	.863		3	4.132	0.00	.935
30	1	4.980	10.18	.986		4	3.742	8.97	.903
	2	4.165	2.00	.910		5	3.605	6.97	.902
	3	4.010	0.00	.909		6	3.458	8.97	.901
	4	3.544	0.00	.865		7	5.061	10.00	.935
	5	4.895	10.00	.909					
	6	3.423	8.18	.868					

(f) Flow conditions.

Figure 6.- Internal flow-field shock diagrams and conditions. $\alpha = 0^{O}$.

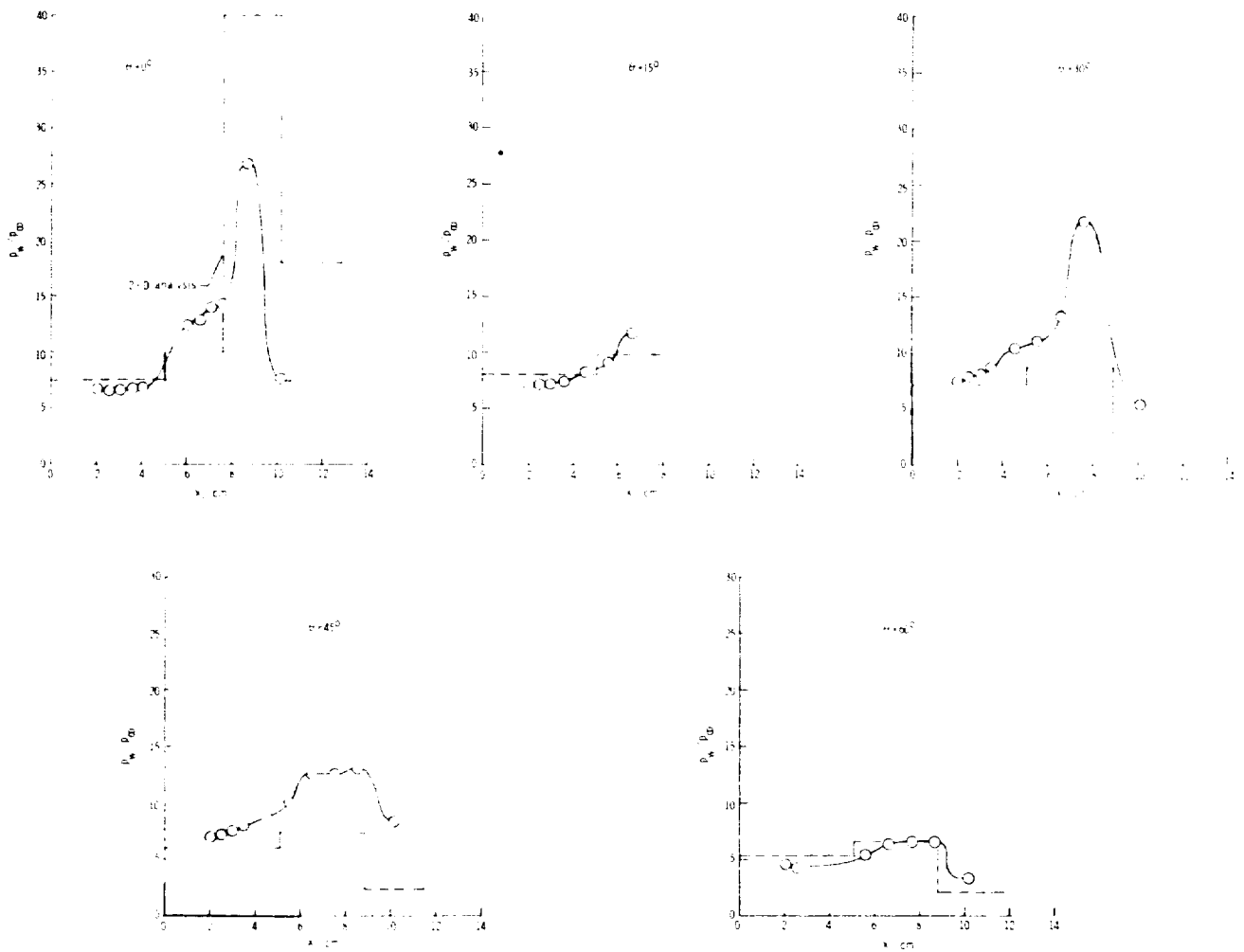

(a) Cowl wall pressure; $\alpha = 0^{O}$.

Figure 7.- Internal wall-pressure distribution.

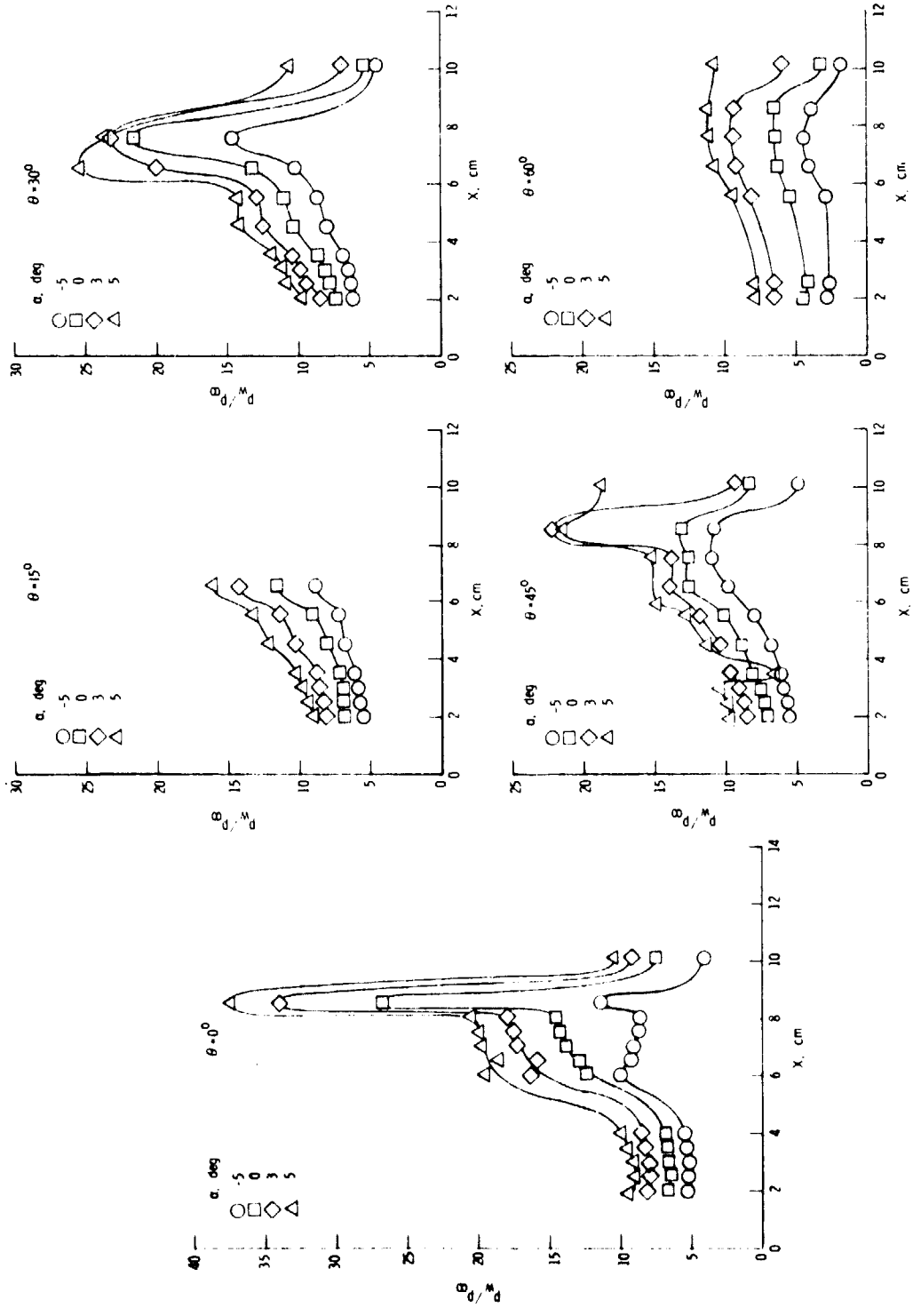

(b) Cowl wall pressure; angle of attack varied.

Figure 7.- Continued.

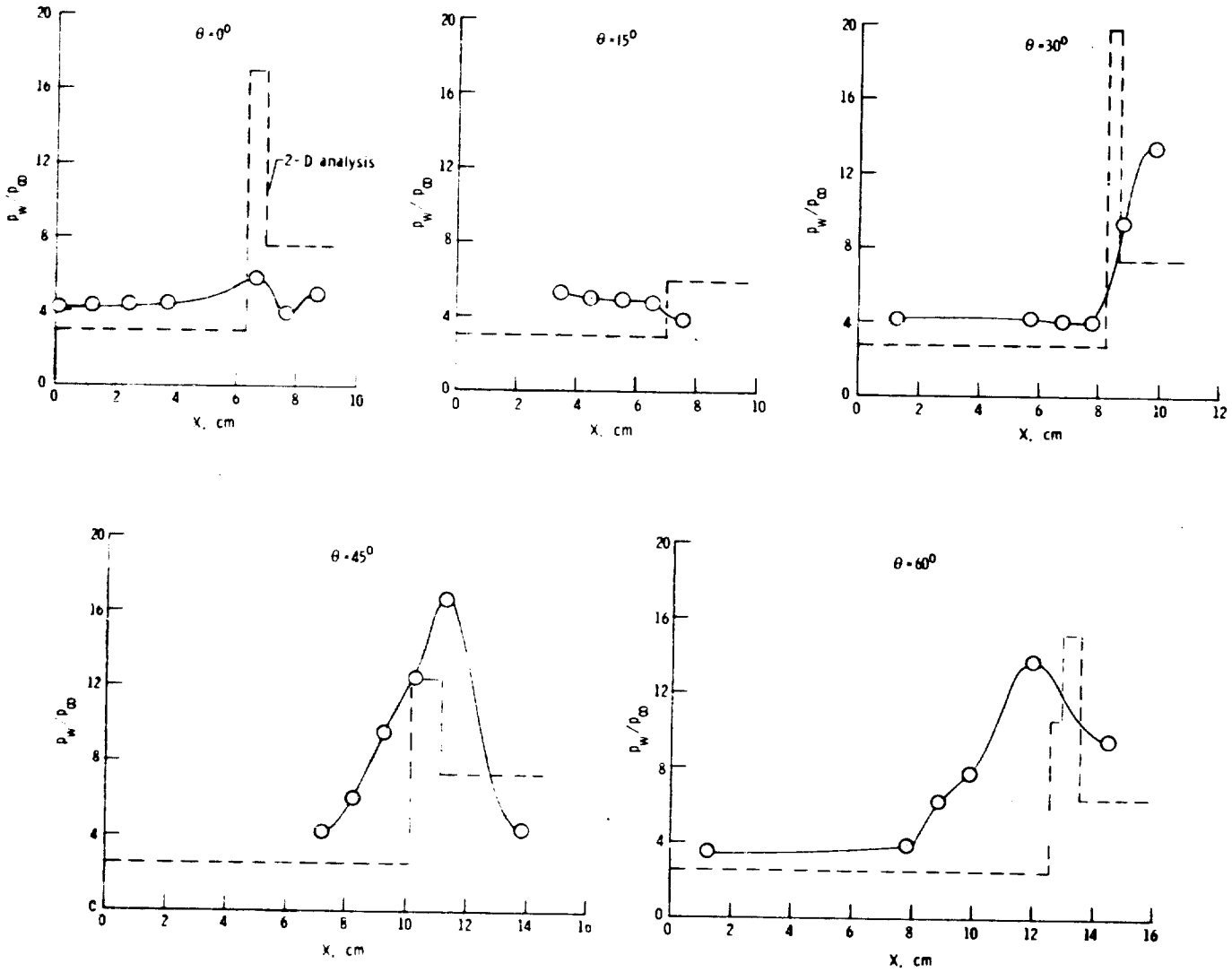

(c) Centerbody wall pressure.

Figure 7.- Continued.

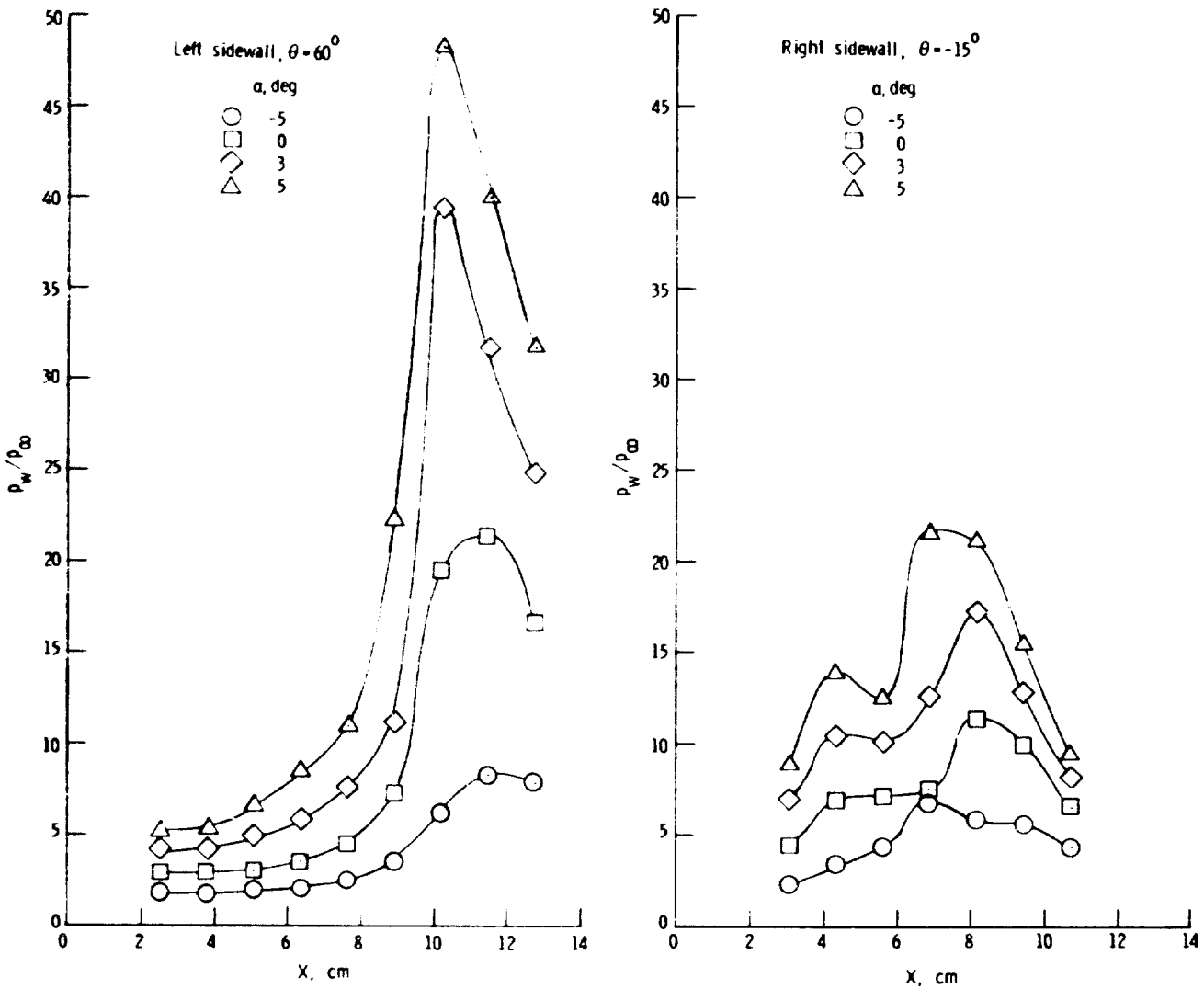

(d) Sidewall pressure.

Figure 7.- Concluded.

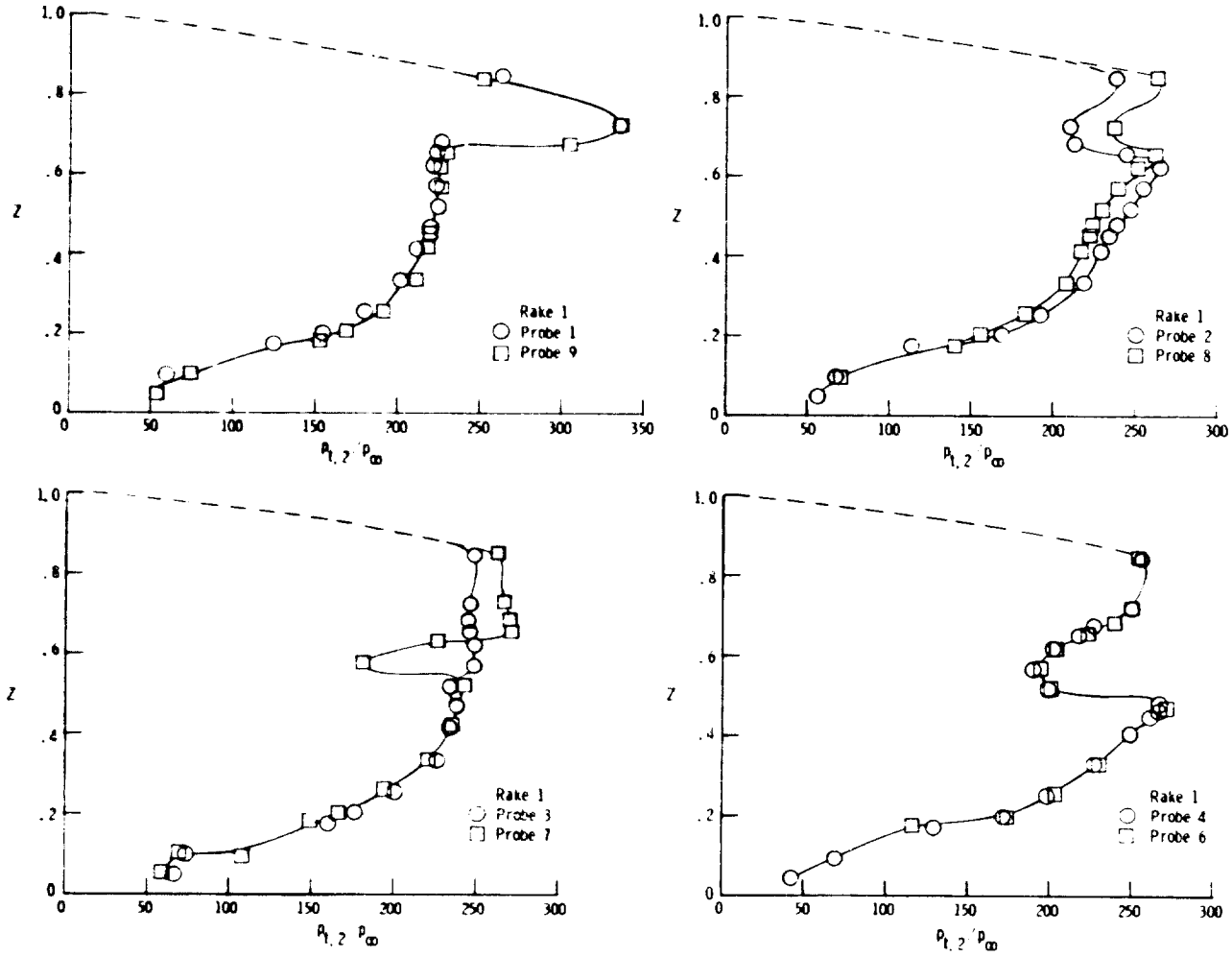

(a) $\theta = 0^{\circ}$; $\alpha = 0^{\circ}$.

Figure 8.- Pitot-pressure survey profiles.

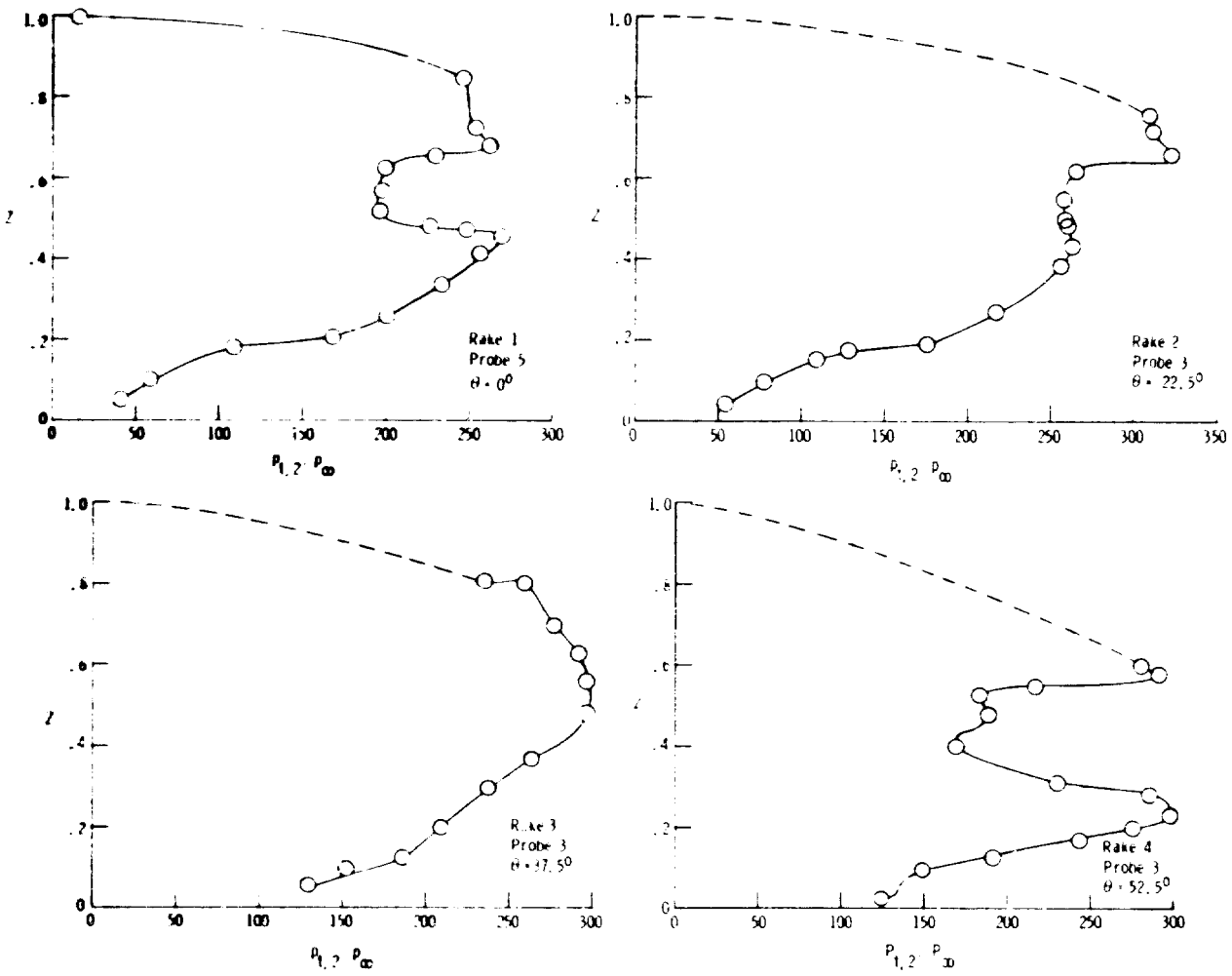

(b) Profiles at each rake position; $\alpha = 0^{O}$.

Figure 8.- Continued.

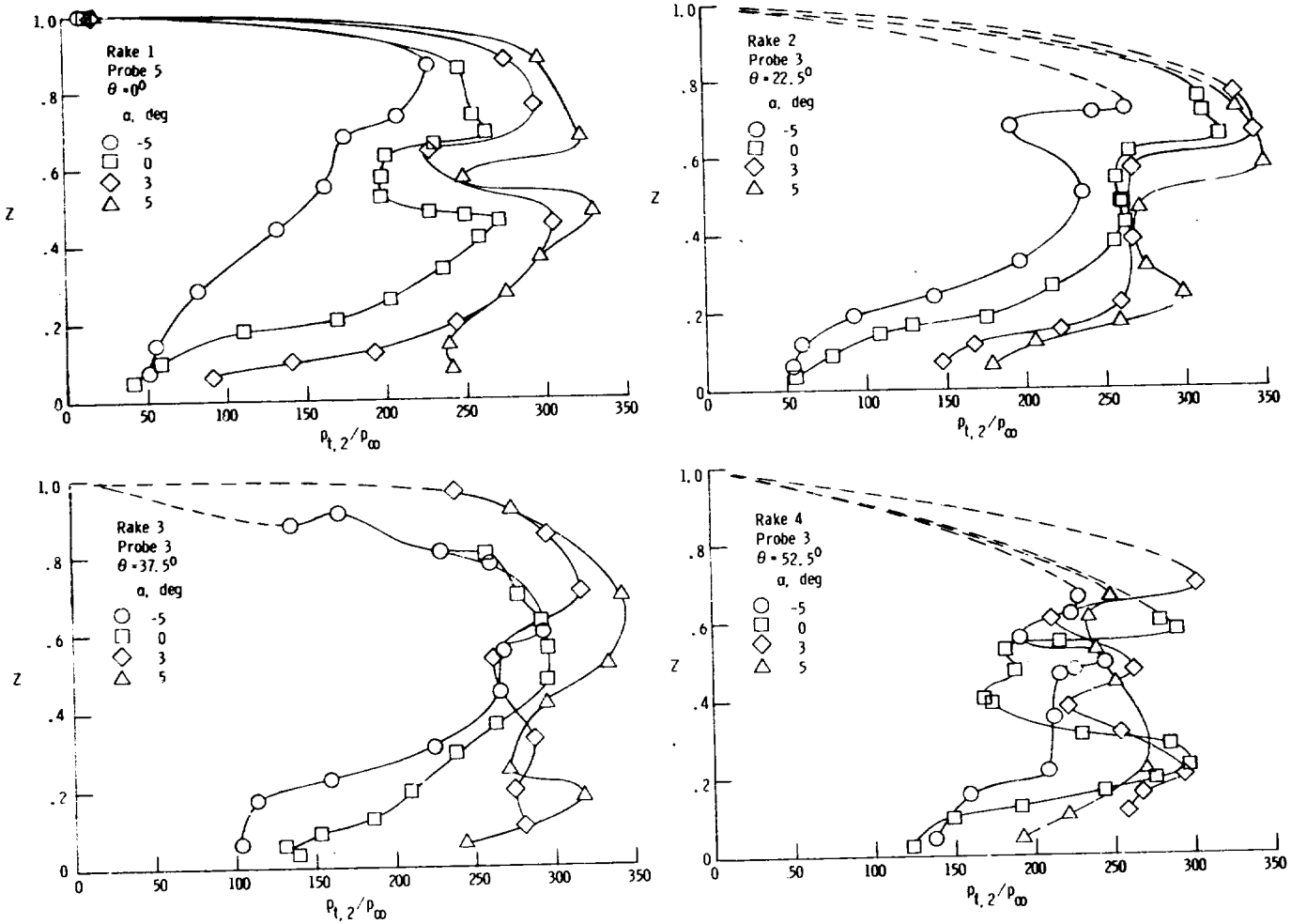

(c) Angle of attack varied.

Figure 8.- Concluded.

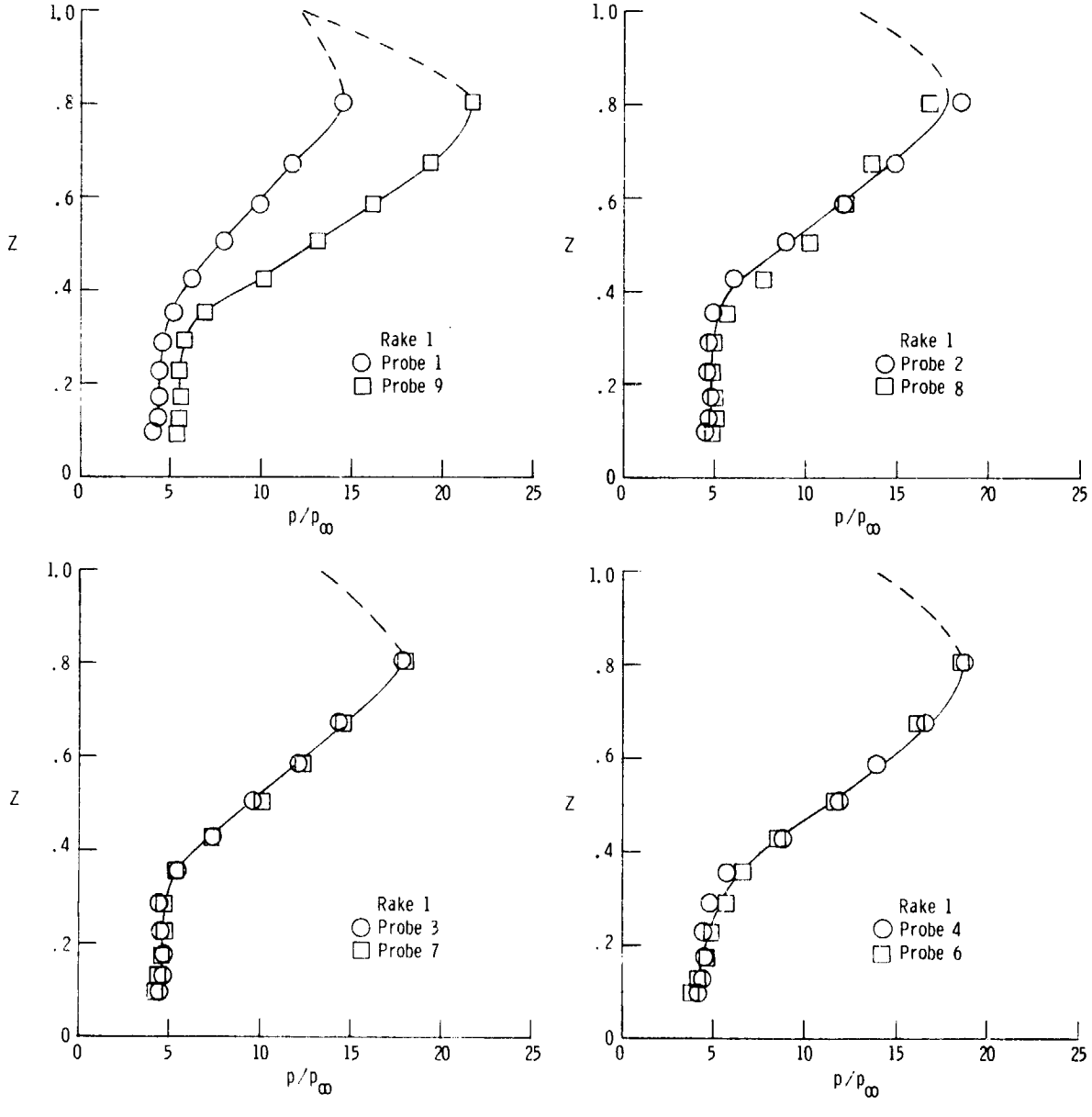

(a) $\theta = 0^{o}$; $\alpha = 0^{o}$.

Figure 9.- Static-pressure survey profiles.

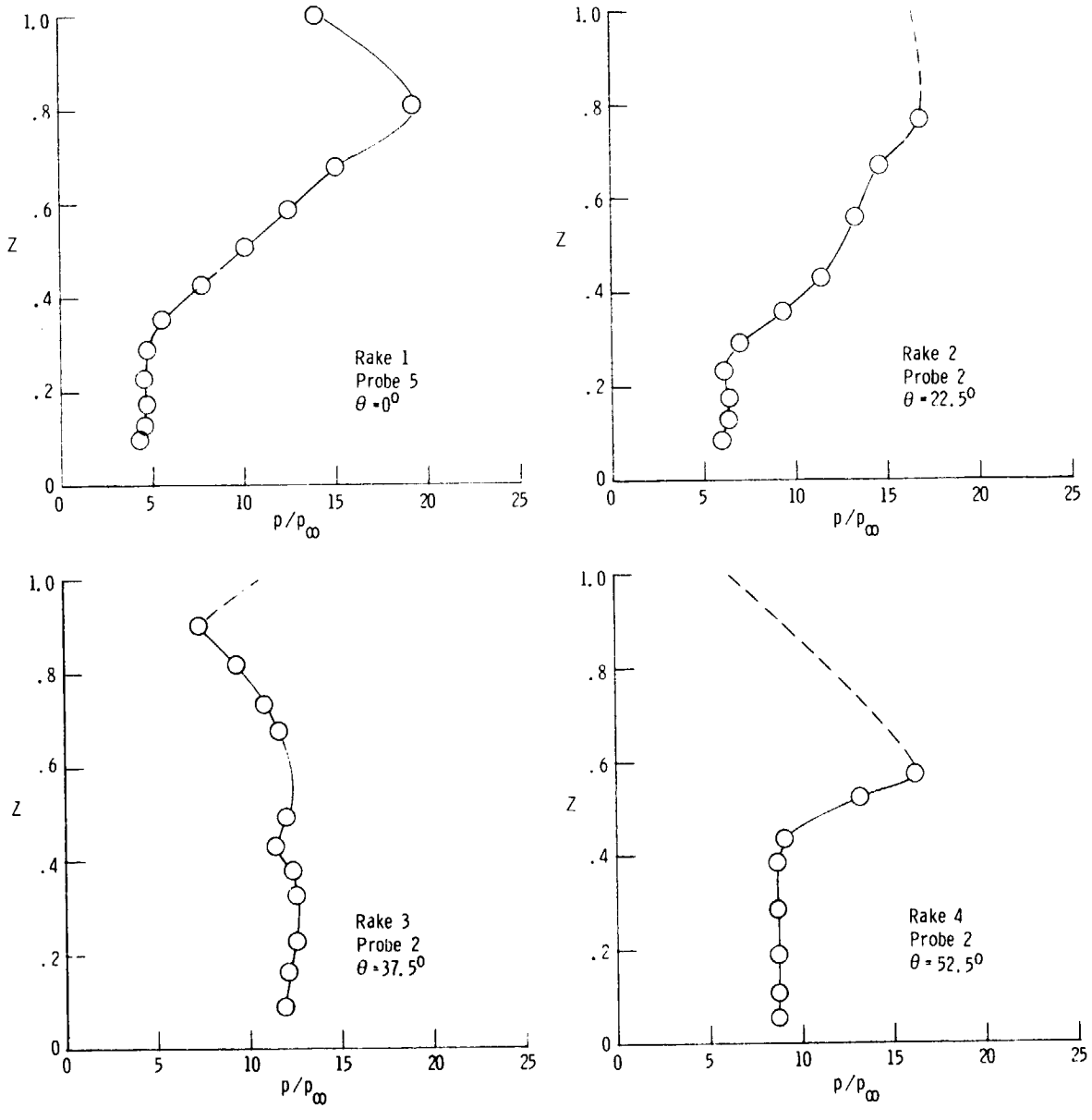

(b) Profiles at each rake position; $\alpha = 0^0$.

Figure 9.- Continued.

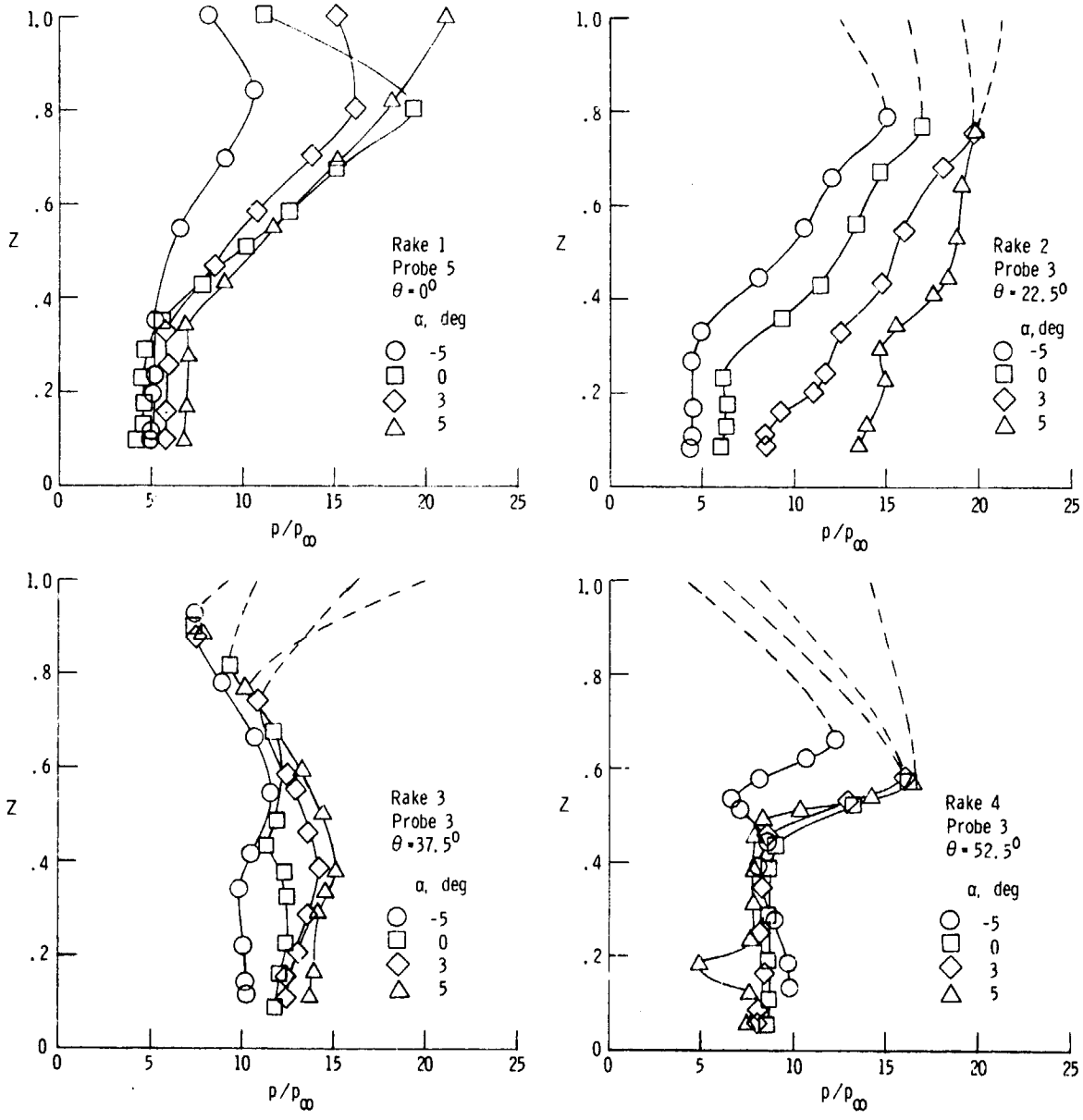

(c) Angle of attack varied.

Figure 9.- Concluded.

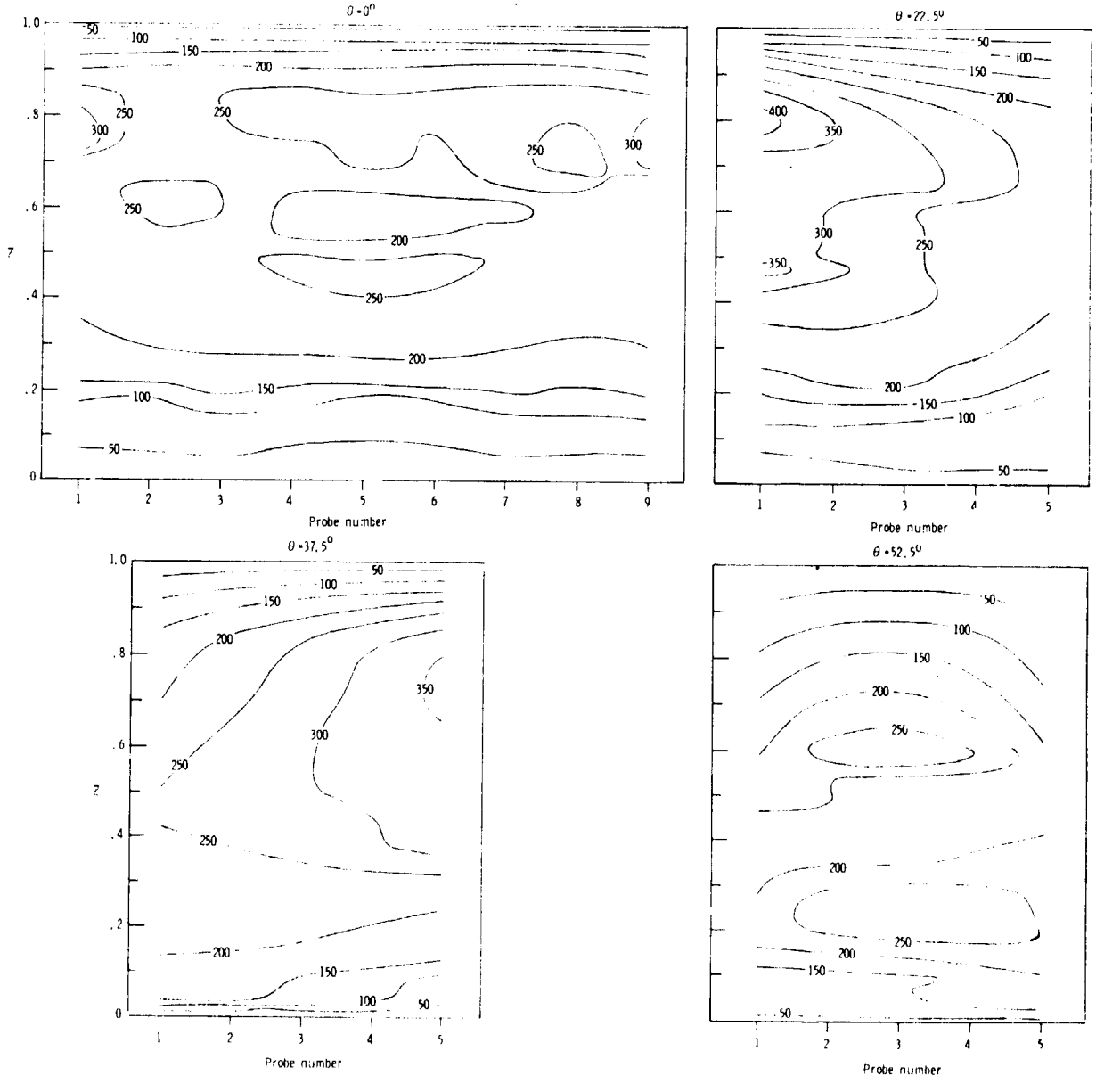

(a) Pitot pressure at each rake position. $\alpha = 0^{o}$.

Figure 10.- Throat-flow parameter contour plots.

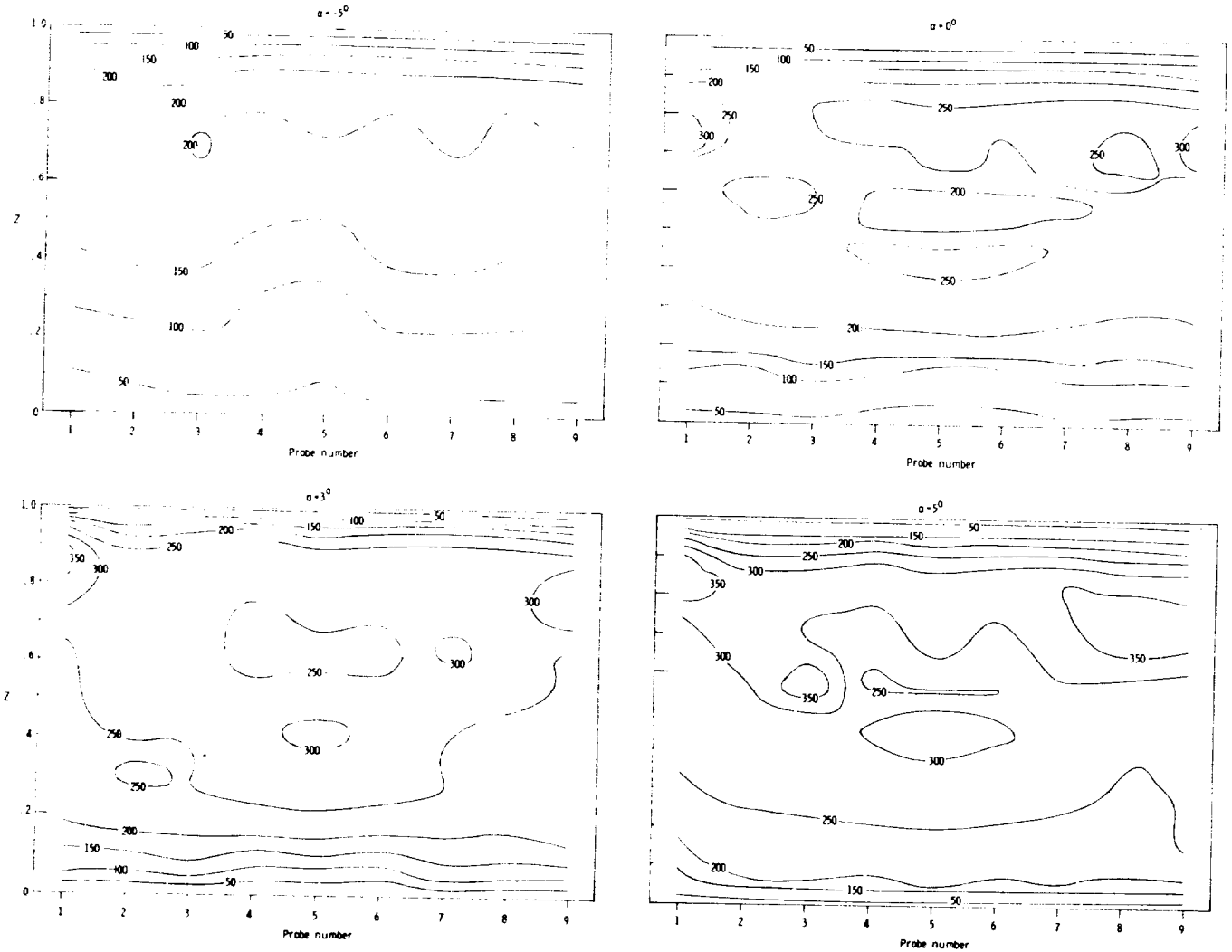

(b) Pitot pressure at $\theta = 0^{\circ}$; angle of attack varied.

Figure 10.- Continued.

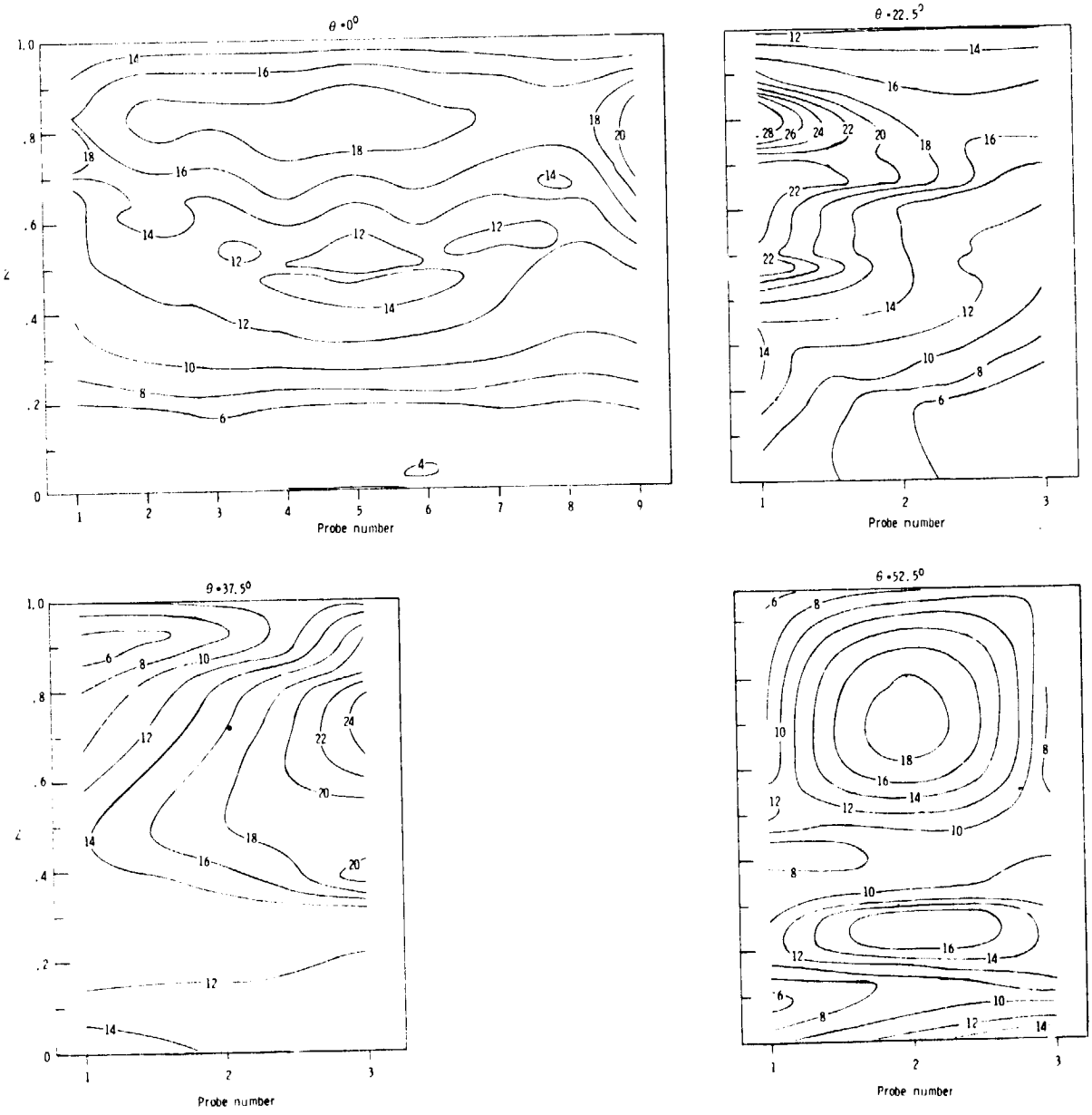

(c) Static pressure at each rake position; $\alpha = 0^{\circ}$.

Figure 10.- Continued.

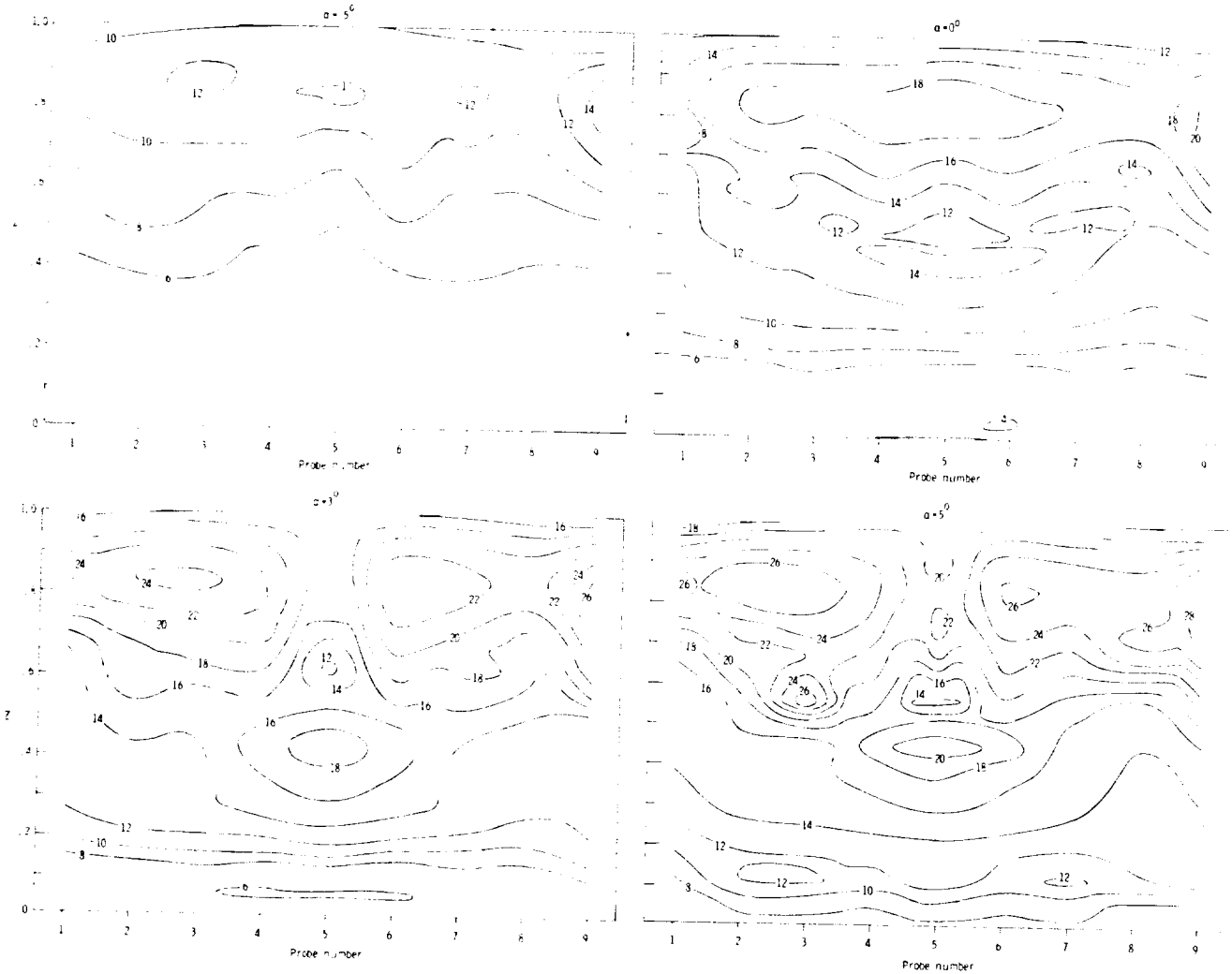

(d) Static pressure at $\theta = 0^{o}$; angle of attack varied.

Figure 10.- Continued.

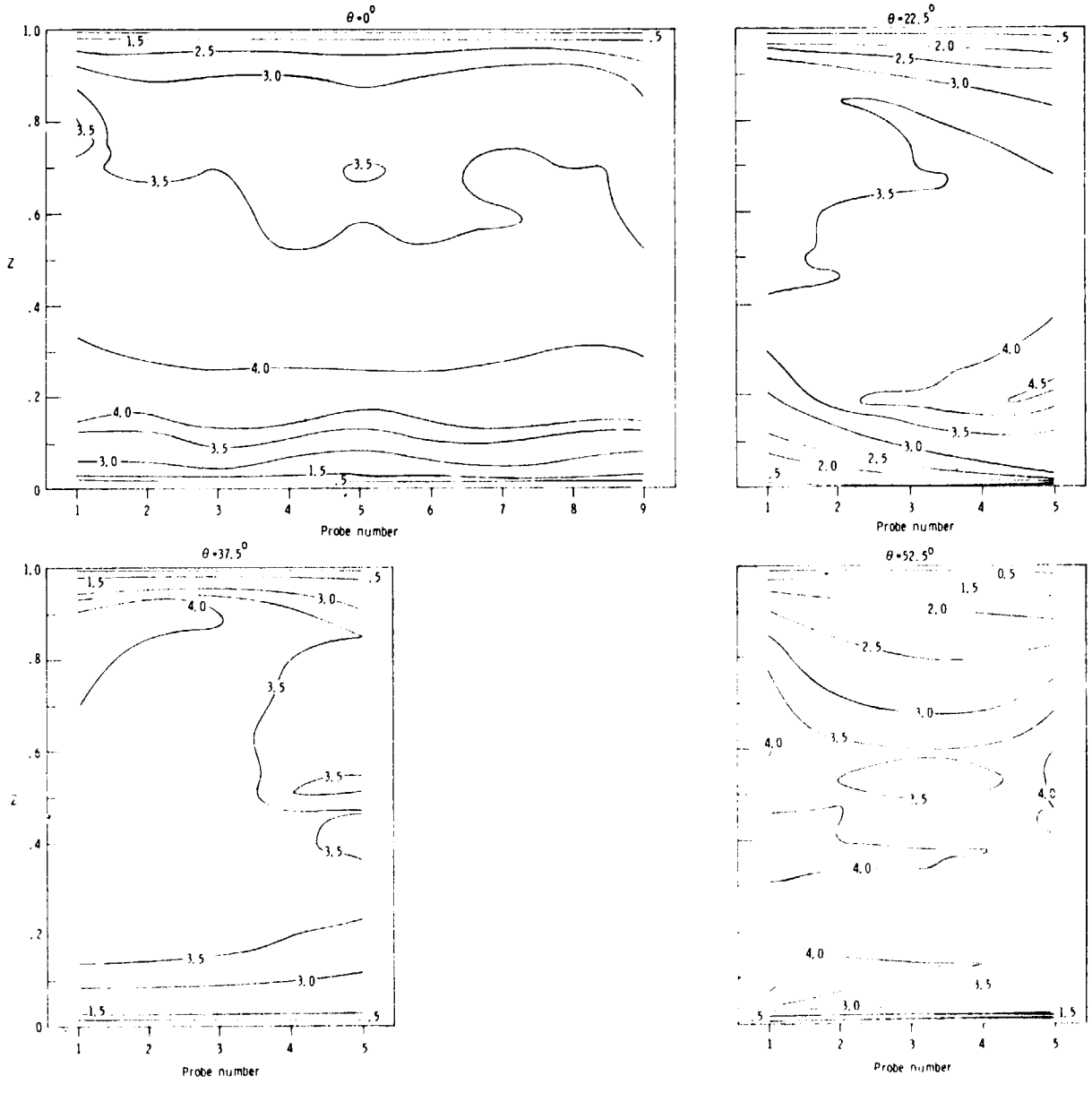

(e) Mach number at each rake position; $\alpha = 0^{\circ}$.

Figure 10.- Continued.

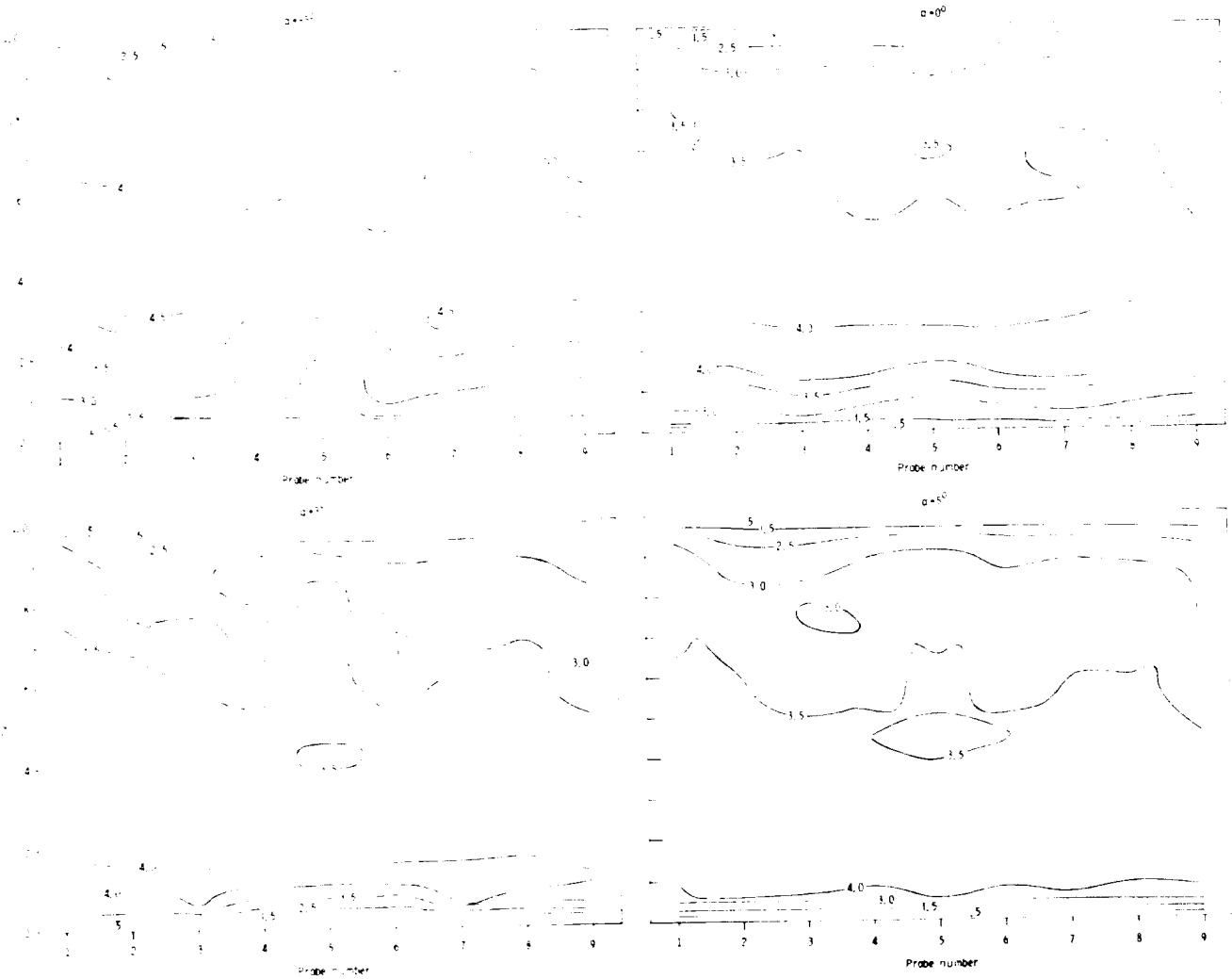

(f) Mach number at $\theta = 0^{o}$; angle of attack varied.

Figure 10.- Continued.

(g) Total pressure recovery at each rake position; $\alpha = 0^{o}$.

Figure 10.- Continued.

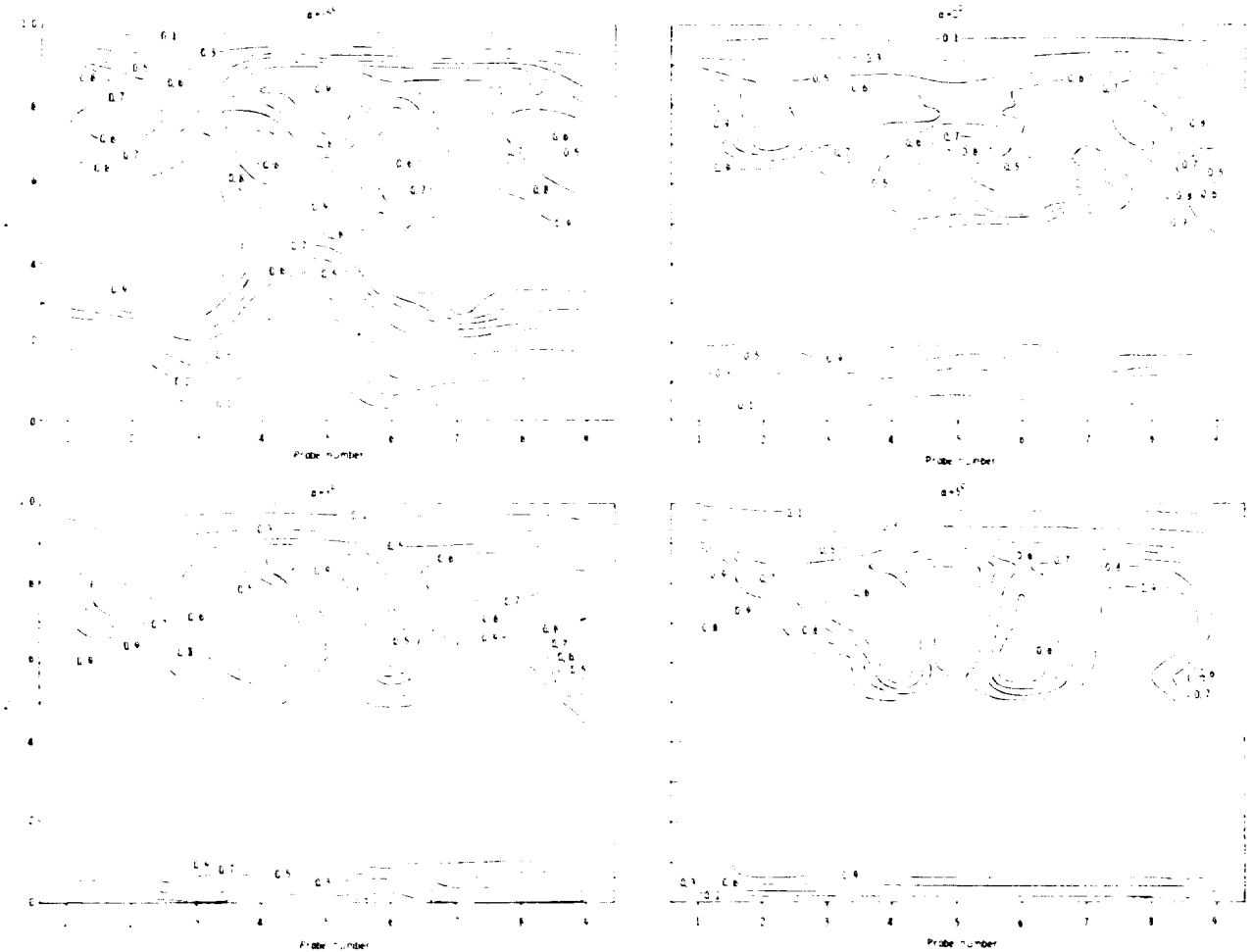

(h) Total pressure recovery at $\theta = 0^{O}$; angle of attack varied.

Figure 10.- Concluded.

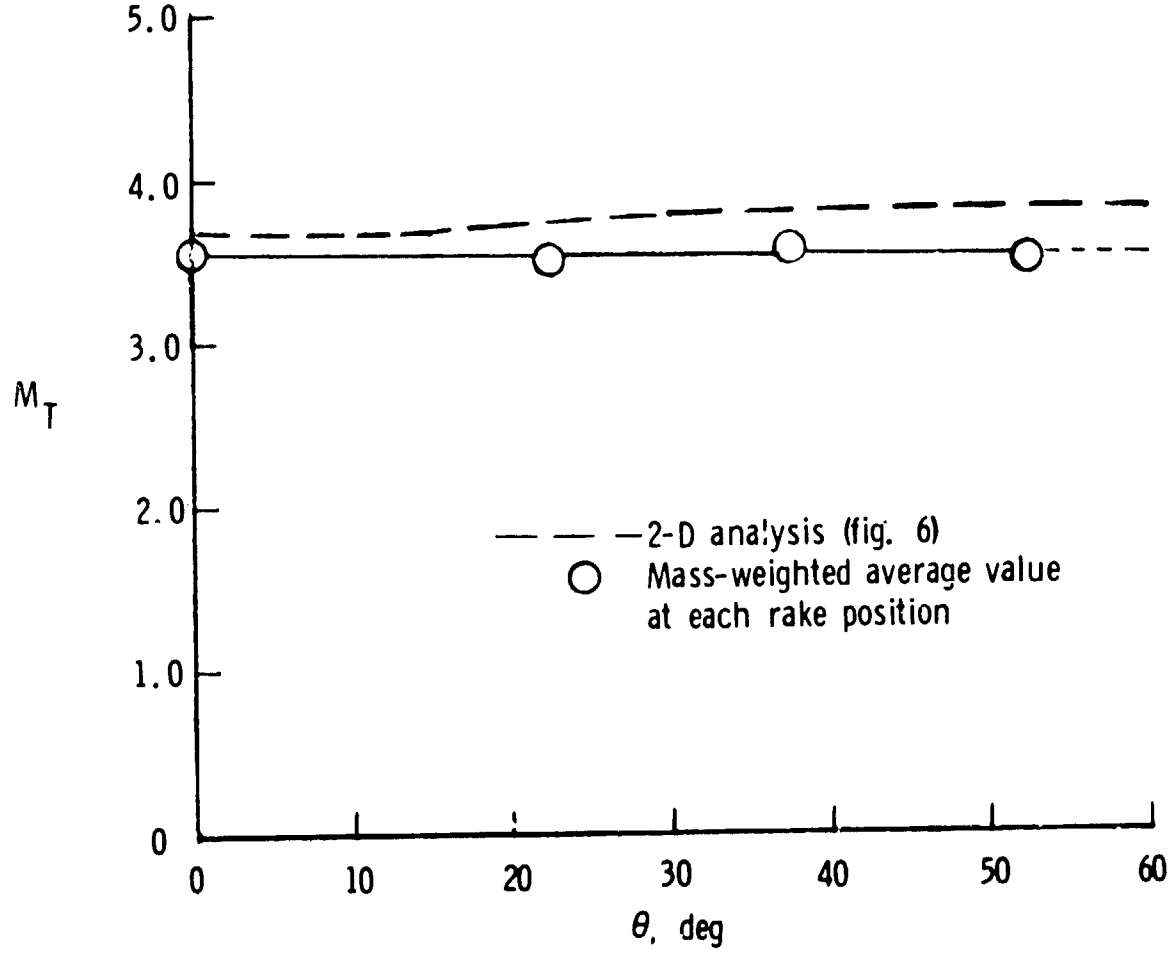

(a) $\alpha = 0^{\circ}$.

Figure 11.- Throat Mach number distribution. $\eta_{D,max} = 0.91$.

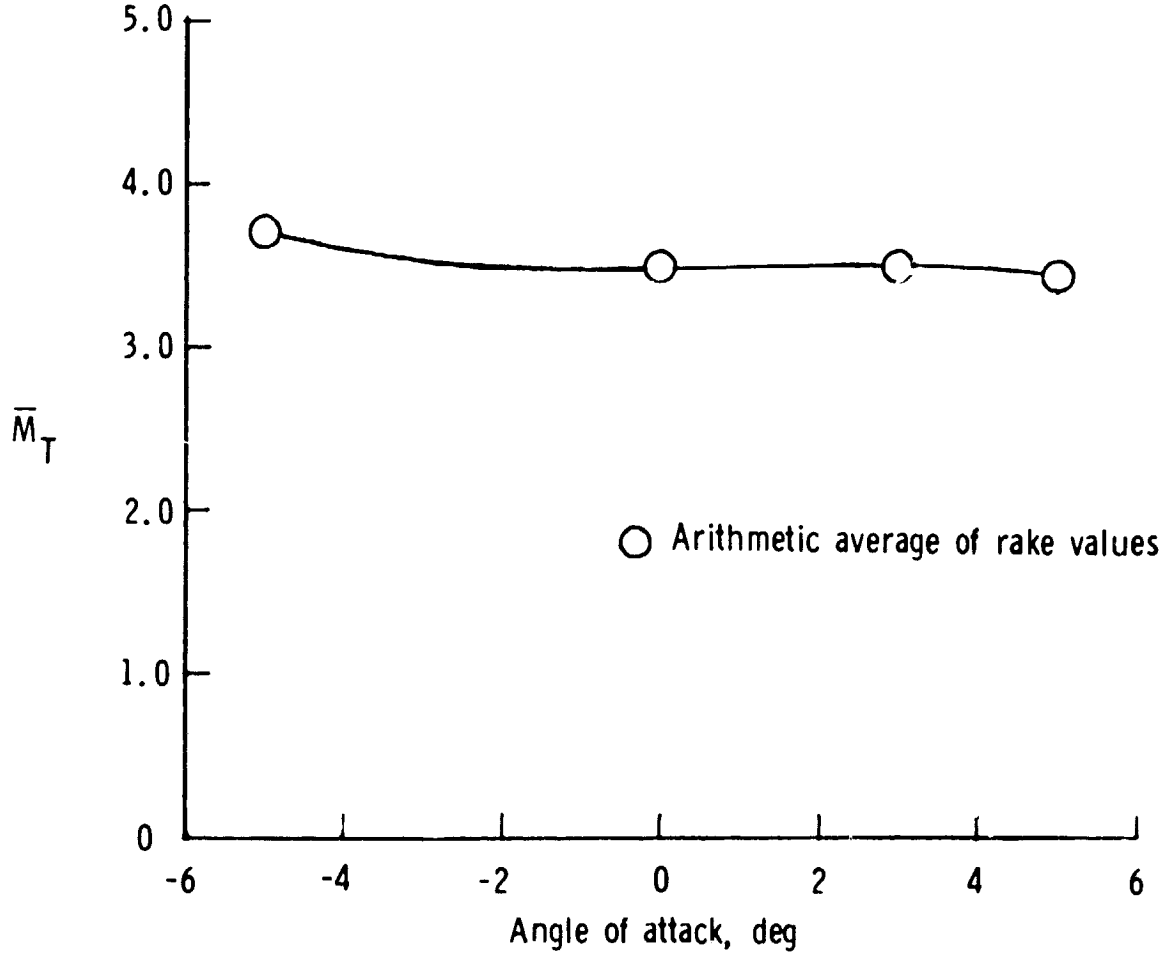

(b) Angle of attack varied.

Figure 11.- Concluded.

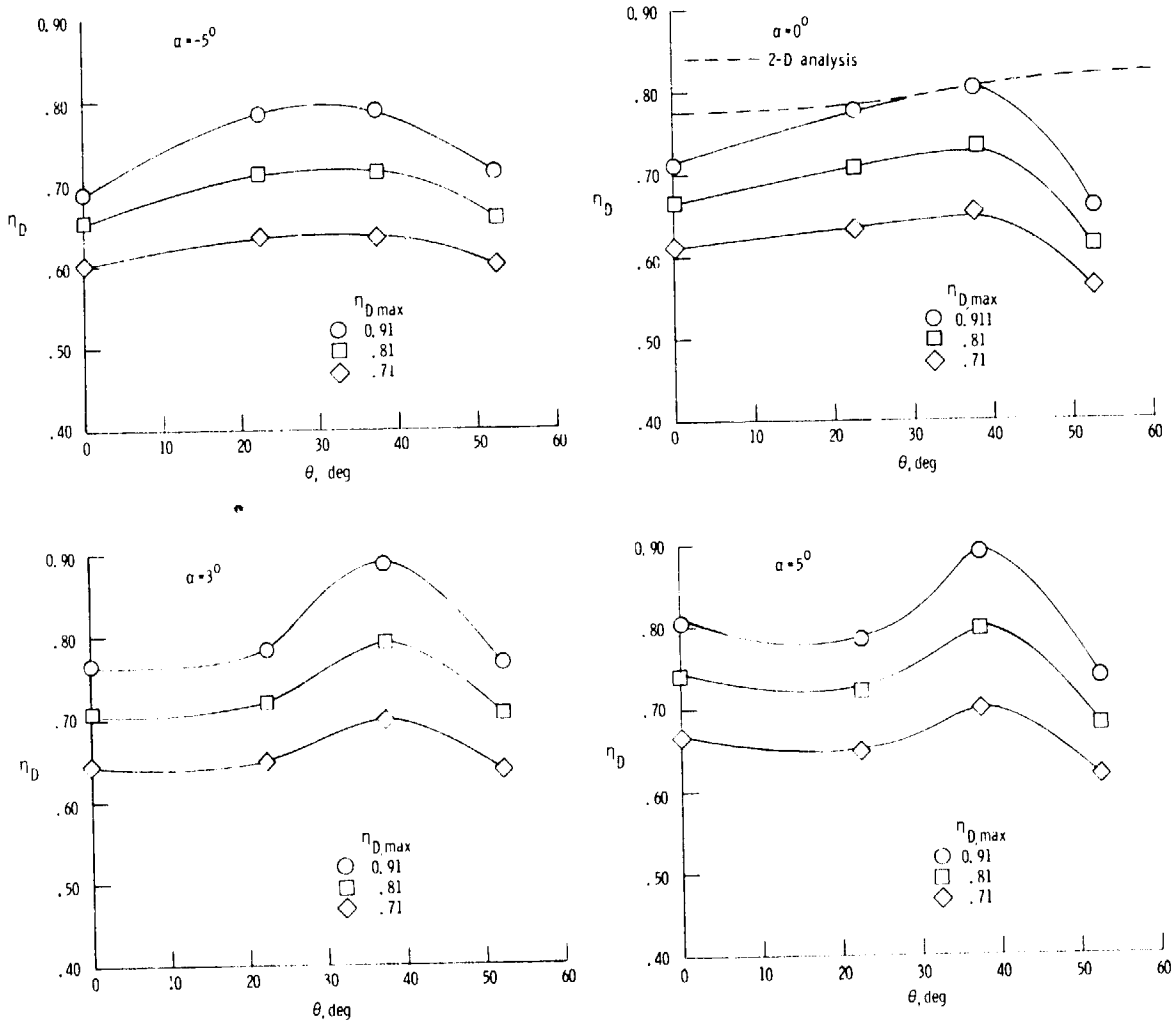

(a) Angle of attack varied.

Figure 12.- Total-pressure recovery distribution.

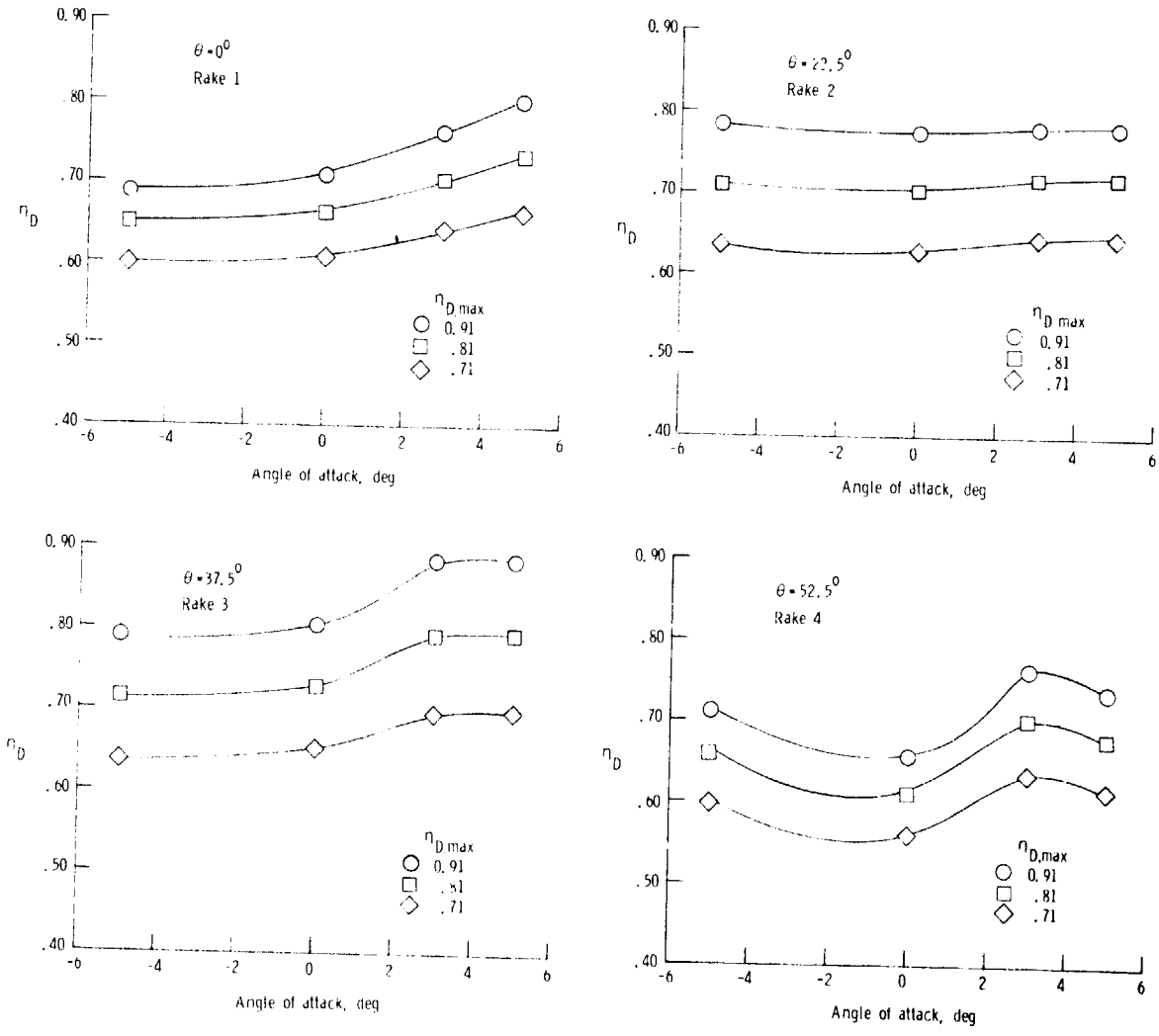

(b) Recovery at each rake position.

Figure 12.- Continued.

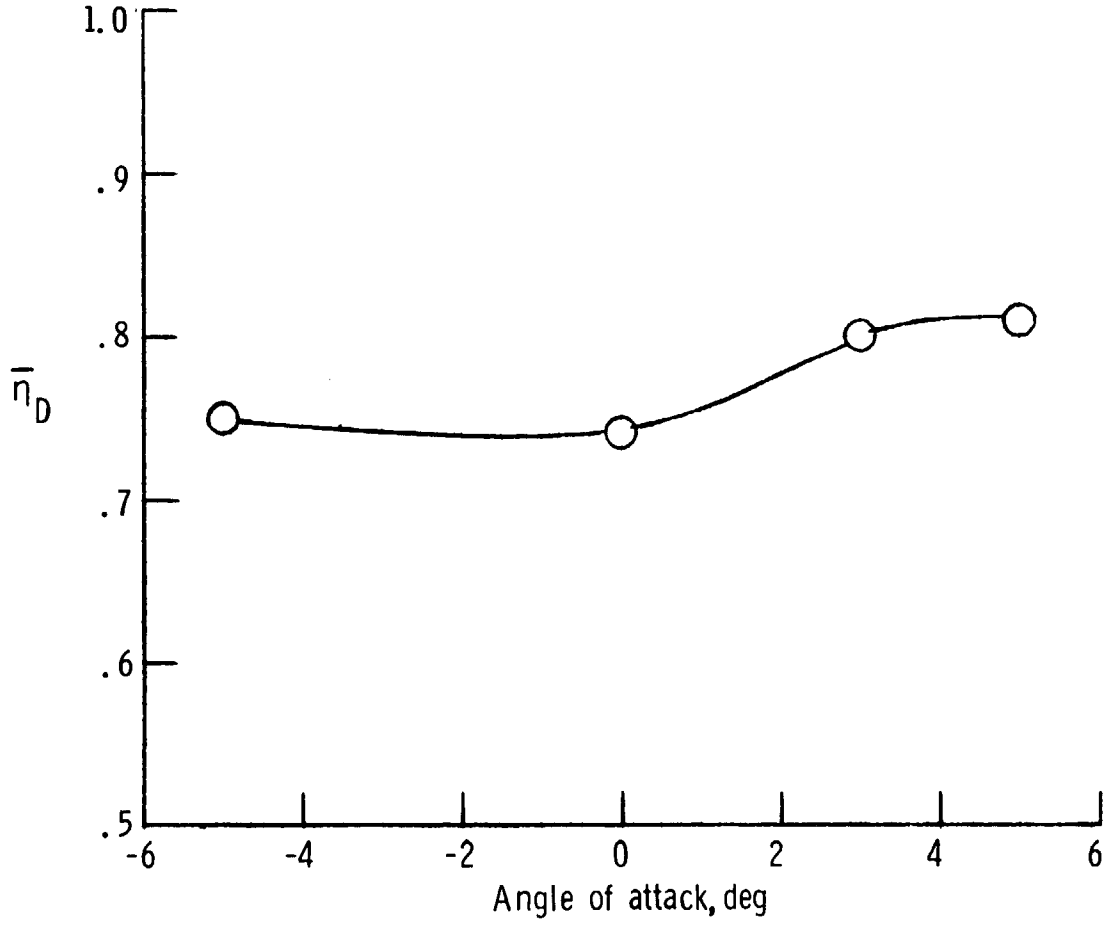

(c) Average recovery; $\eta_{D,max} = 0.91$.

Figure 12.- Concluded.

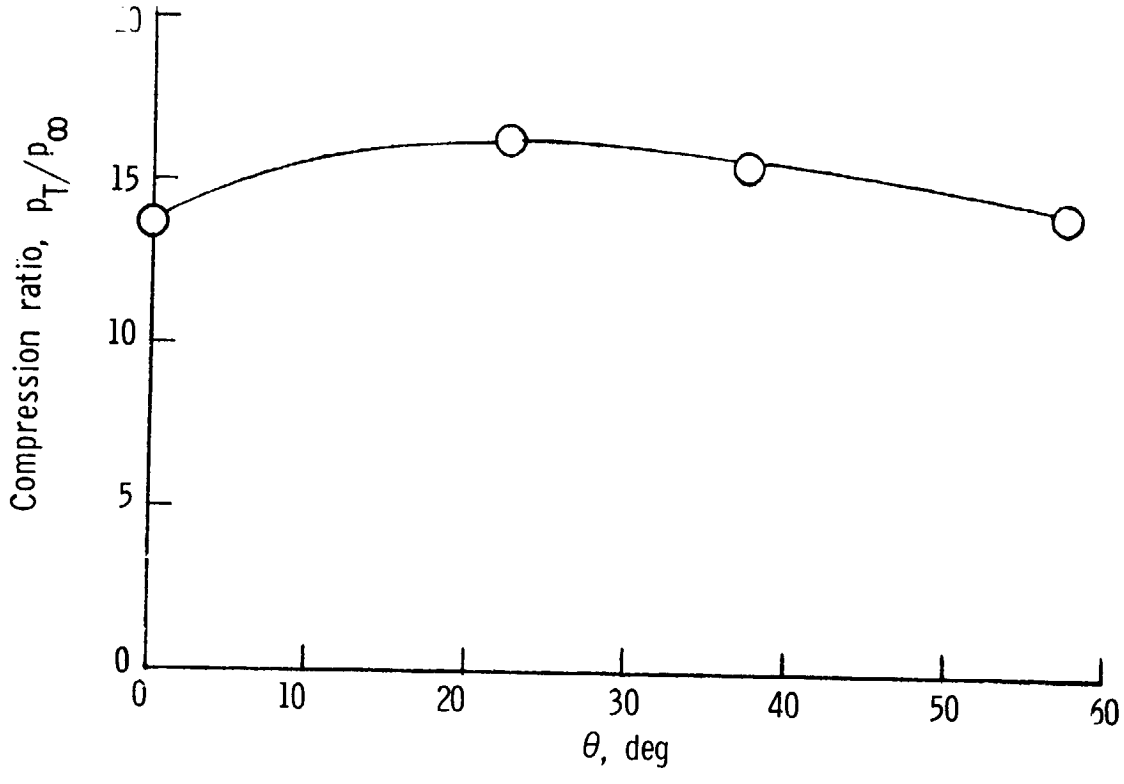

(a) $\alpha = 0^o$.

Figure 13.- Static-pressure compression-ratio distribution. $\eta_{D,max} = 0.91$.

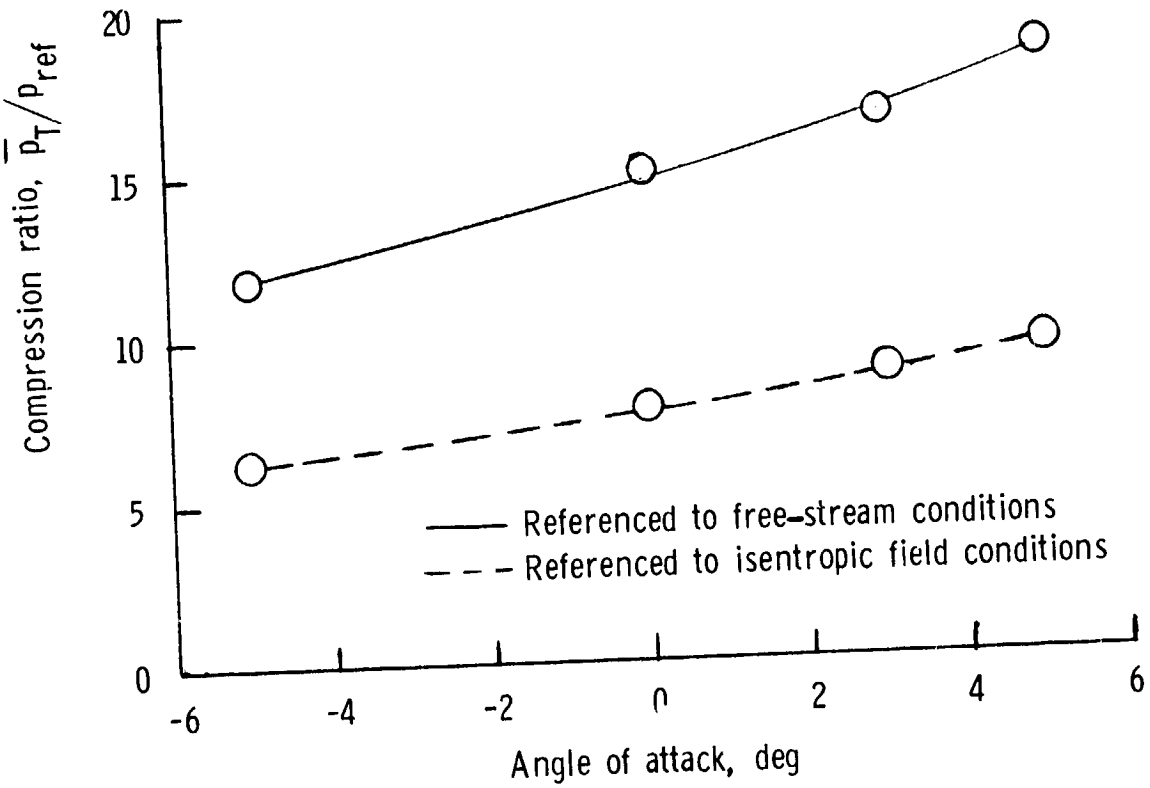

(b) Angle of attack varied.

Figure 13.- Concluded.

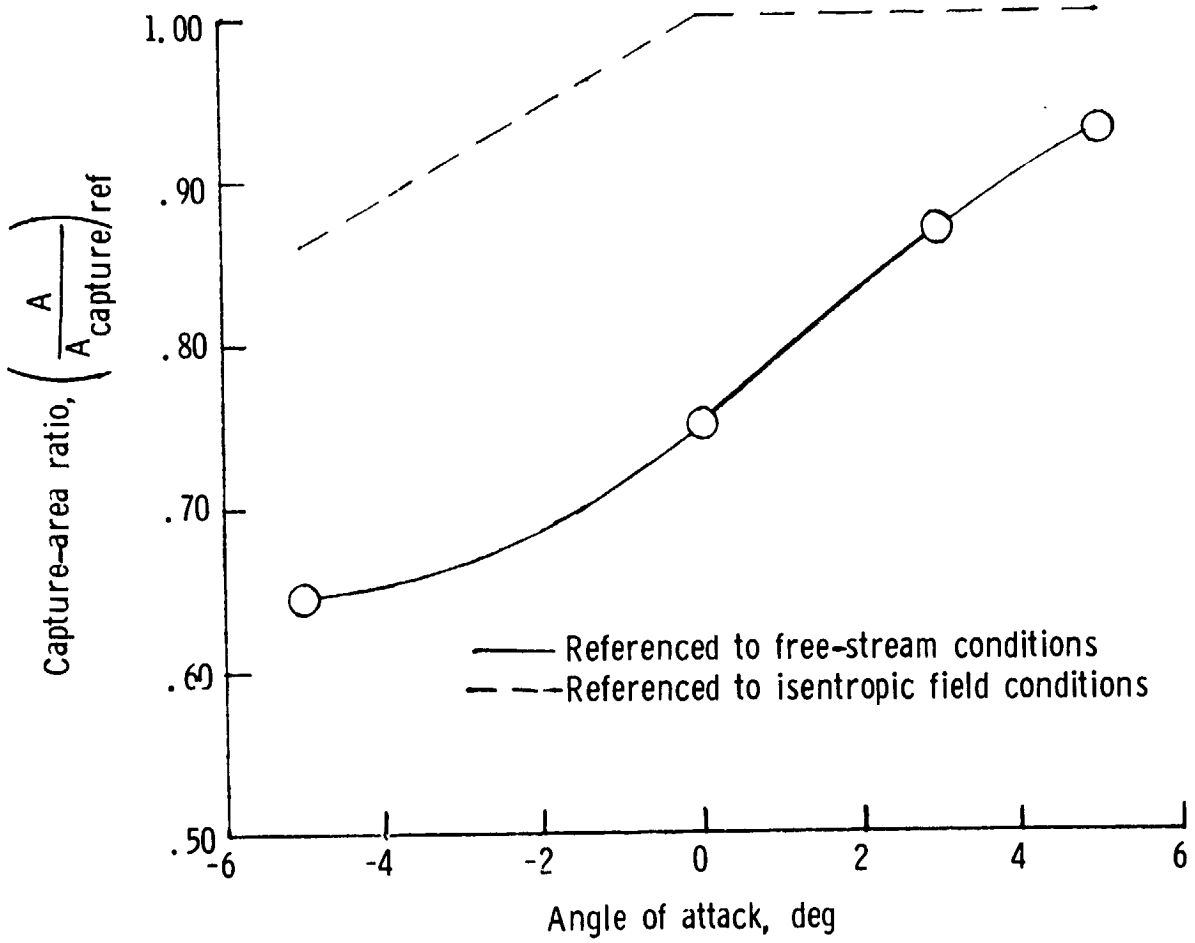

Figure 14.- Capture area ratio. $\eta_{D,max} = 0.91$

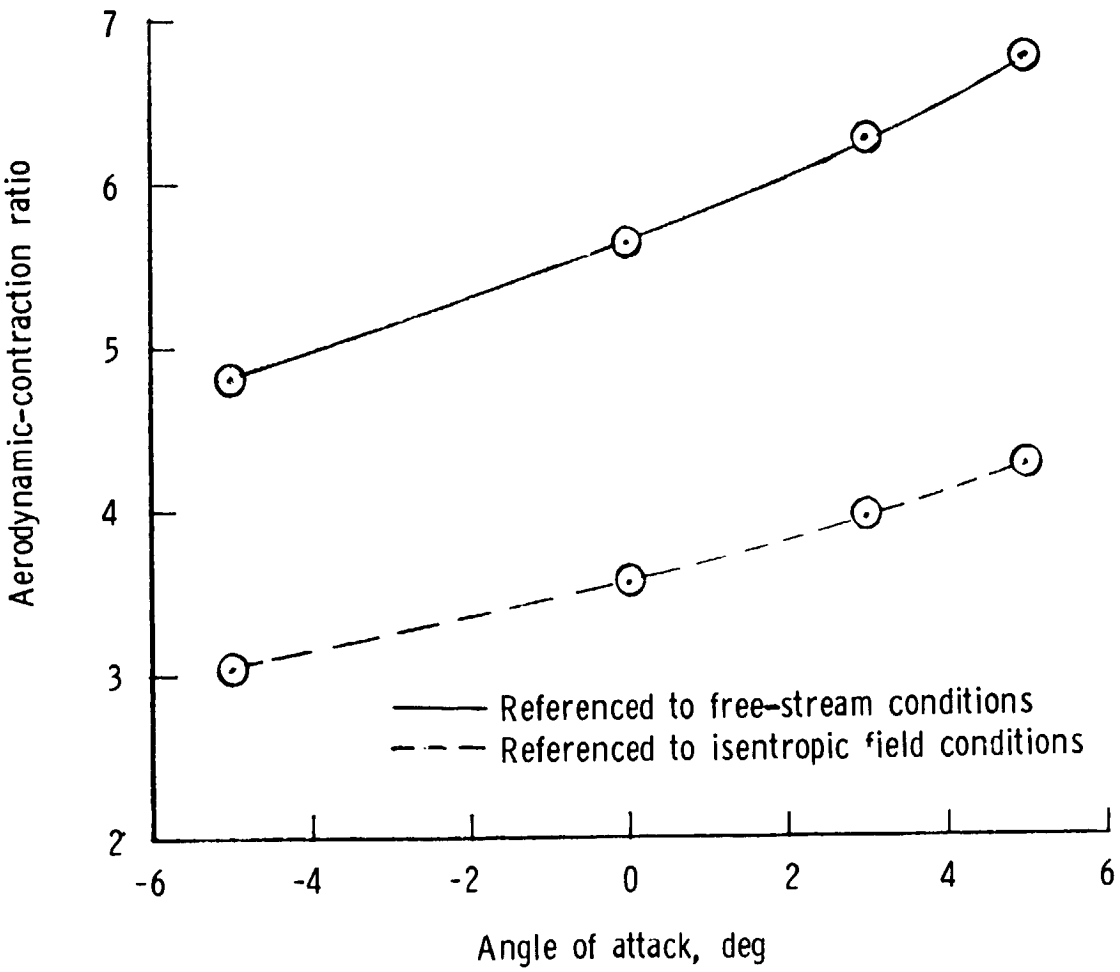

Figure 15.- Aerodynamic-contraction ratio. $\eta_{D,max} = 0.91$.